

Study of conservation and recurrence of Runge-Kutta discontinuous Galerkin schemes for Vlasov-Poisson systems

Yingda Cheng ^{*} Irene M. Gamba [†] Philip J. Morrison [‡]

August 13, 2018

Abstract

In this paper we consider Runge-Kutta discontinuous Galerkin (RKDG) schemes for Vlasov-Poisson systems that model collisionless plasmas. One-dimensional systems are emphasized. The RKDG method, originally devised to solve conservation laws, is seen to have excellent conservation properties, be readily designed for arbitrary order of accuracy, and capable of being used with a positivity-preserving limiter that guarantees positivity of the distribution functions. The RKDG solver for the Vlasov equation is the main focus, while the electric field is obtained through the classical representation by Green's function for the Poisson equation. A rigorous study of recurrence of the DG methods is presented by Fourier analysis, and the impact of different polynomial spaces and the positivity-preserving limiters on the quality of the solutions is ascertained. Several benchmark test problems, such as Landau damping, the two-stream instability, and the KEEN (Kinetic Electro static Electron Nonlinear) wave, are given.

Keywords: Vlasov-Poisson, discontinuous Galerkin methods, recurrence, positivity-preserving, BGK mode, KEEN wave.

1 Introduction

The Vlasov-Poisson (VP) system is an important equation for modeling collisionless plasmas, one that possesses computational difficulties of more complete kinetic theories. Thus, it serves as an important test bed for algorithm development. The VP system describes the evolution of $f = f(x, v, t)$, the probability distribution function (*pdf*) for finding an electron (at position x with velocity v at time t) with a uniform background of fixed ions under a self-consistent

^{*}Department of Mathematics, Michigan State University, East Lansing, MI 48824 U.S.A.
ycheng@math.msu.edu

[†]Department of Mathematics and ICES, University of Texas at Austin, Austin, TX 78712 U.S.A.
gamba@math.utexas.edu

[‡]Department of Physics and Institute for Fusion Studies, University of Texas at Austin, Austin, TX 78712 U.S.A. morrison@physics.utexas.edu

electrostatic field. In particular, the non-dimensionalized VP system (with time scaled by the inverse plasma frequency ω_p^{-1} and length scaled by the Debye length λ_D) is given by

$$\begin{aligned} \partial_t f + v \cdot \nabla_x f - E \cdot \nabla_v f &= 0 & \Omega \times (0, T] \\ -\Delta_x \Phi &= 1 - \int_{\mathbb{R}^n} f dv & \Omega_x \times (0, T] \\ E &= -\nabla_x \Phi & \Omega_x \times (0, T]. \end{aligned} \quad (1)$$

Here the domain $\Omega = \Omega_x \times \mathbb{R}^n$, where Ω_x can be either a finite domain or \mathbb{R}^n . The boundary conditions for the above systems are summarized as follows: $f \rightarrow 0$ as $|x| \rightarrow \infty$ or $|v| \rightarrow \infty$. If Ω_x is finite, then we can impose either inflow boundary conditions with $f = f^{in}$ on $\Gamma_I = \{(x, v) | v \cdot \nu_x < 0\}$, where ν_x is the outward normal vector, or more simply impose periodic boundary conditions. For simplicity of discussion, in this paper, we will always assume periodicity in x . Also, we add that when the VP system is applied to plasmas the total charge neutrality condition, $\int_{\Omega_x} \left(\int_{\mathbb{R}^n} f dv - 1 \right) dx = 0$, is imposed.

The following physical quantities associated with this system are related to its conservation properties:

$$\begin{aligned} \text{charge density} \quad \rho(x, t) &= \int_{\mathbb{R}^n} f(x, v, t) dv, \\ \text{momentum density} \quad j(x, t) &= \int_{\mathbb{R}^n} v f(x, v, t) dv, \\ \text{kinetic energy density} \quad \xi_k(x, t) &= \frac{1}{2} \int_{\mathbb{R}^n} |v|^2 f(x, v, t) dv, \\ \text{electrostatic energy density} \quad \xi_e(x, t) &= \frac{1}{2} |E(x, t)|^2. \end{aligned} \quad (2)$$

Indeed, it is well-known that the VP system conserves the total electron charge $\int_{\Omega_x} \rho(x) dx$, momentum $\int_{\Omega_x} j(x) dx$, and energy $\int_{\Omega_x} (\xi_k(x) + \xi_e(x)) dx$. Moreover, any functional of the form $\int_{\Omega} G(f) dx dv$ is a constant of motion. In particular, this includes the k -th order invariant $I_k = \int_{\Omega} f^k dx dv$ and the entropy $S = -\int_{\Omega} f \ln(f) dx dv$. Sometimes the functional I_2 is also called the enstrophy, and all of these invariants are called Casimir invariants (see, e.g., [34]).

The VP system has been studied extensively for the simulation of collisionless plasmas. Popular numerical approaches include Particle-In-Cell (PIC) methods [6, 24], Lagrangian particle methods [4, 17], semi-Lagrangian methods [8, 45], the WENO method coupled with Fourier collocation [58], finite volume (flux balance) methods [7, 18, 19], Fourier-Fourier spectral methods [27, 28], continuous finite element methods [49, 50], among many others. In this paper, we will focus on the discontinuous Galerkin (DG) method to solve the VP system. The original DG method was introduced by Reed and Hill [42] for neutron transport. Lesaint and Raviart [32] performed the first convergence study for the original DG method. Cockburn and Shu in a series of papers [14, 13, 12, 11, 15] developed the Runge-Kutta DG (RKDG) method for hyperbolic equations. The RKDG methods have been used to simulate the VP system in plasmas by Heath, Gamba, Morrison and Michler [23, 22] and for the gravitational infinite homogeneous stellar system by Cheng and Gamba [9]. Theoretical aspects about stability, accuracy and conservation of those methods are discussed in [22, 23] and more recently in [3, 2]

for energy conserving schemes. Such methods have excellent conservation properties, can be readily designed for arbitrary order of accuracy, and have the potential for implementation on unstructured meshes with hp -adaptivity. To ensure the positivity of the solution, one can use a maximum-principle-satisfying limiter that has been recently proposed by Zhang and Shu in [52] for conservation laws on cartesian meshes, and later extended on triangular meshes [56]. This limiter has been used to develop positivity-preserving schemes for compressible Euler [53, 55], shallow water equations [48], and Vlasov-Boltzmann transport equations [10]. It has also been employed recently in the framework of semi-Lagrangian DG methods [43, 41] for the VP system.

The scope of the present paper is as follows: we focus on a detailed study of the RKDG scheme for the Vlasov equation from both the numerical and analytical points of view. Since we are only considering one-dimensional problems, we use the classical representation of the solution by Green's function to compute the Poisson equation; therefore, the electric field is explicitly given as a function of the numerical density. This removes all discretization error from the Poisson equation and lets us more accurately investigate our DG solver for the Vlasov equations. We rigorously study recurrence, which is an important numerical phenomenon that commonly appears with many solvers. We use Fourier analysis and obtain eigenvalues of the amplification matrix, and then investigate the impact of different polynomial spaces on the quality of the solution by examining conserved quantities as well as convergence to BGK states [5] for some choices of initial states. We consider benchmark test problems such as simulations of Landau damping phenomena for the linearized and nonlinear Vlasov Poisson systems, two-stream instability, and their long time BGK states and the formation of KEEN waves, both for the nonlinear system as well.

The remaining part of the paper is organized as follows: in Section 2, we describe the numerical algorithm and summarize its conservation properties. In Section 3, we study the recurrence phenomena that occurs for linear Vlasov type transport equations discretized by DG methods with various polynomial orders. Sections 4.1 and 4.2 are devoted to discussions of simulation results for the linearized and nonlinear VP system, respectively, for diverse choices of initial data and external drive potentials. We conclude with a few remarks in Section 5.

2 Numerical methods

In this section we first describe the proposed DG numerical algorithm and then discuss some of its basic conservation properties related to the quantities of (2). This is done for both the fully nonlinear VP system of (1) and the linearized VP system obtained by linearizing about the homogeneous equilibrium $f_{eq}(v)$, with corresponding vanishing electric equilibrium field. Periodic boundary conditions in x are assumed.

Thus, setting $f(x, v, t) = f_{eq}(v) + \delta f(x, v, t)$ and expanding the system to first order approximation, the perturbation δf satisfies the Linear Vlasov-Poisson (LVP) system,

$$\begin{aligned} \partial_t f + v \cdot \nabla_x f &= E \cdot \nabla_v f_{eq} & \Omega \times (0, T] \\ \Delta_x \Phi &= \int_{\mathbb{R}^n} f dv & \Omega_x \times (0, T] \\ E &= -\nabla_x \Phi & \Omega_x \times (0, T], \end{aligned} \tag{3}$$

where δf has been replaced by f to ease the notation. We find it convenient and efficient to intertwine the discussion of our algorithms for the VP and LVP systems. To avoid confusion in Section 2.1 we underline the words linear and nonlinear, signaling where discussions specific to each apply.

2.1 Numerical algorithm

For one-dimensional problems, we use a mesh that is a tensor product of grids in the x and v directions, because this simplifies the definitions of the mesh and polynomial space for the Poisson equation. Specifically, the domain Ω is partitioned as follows:

$$0 = x_{\frac{1}{2}} < x_{\frac{3}{2}} < \dots < x_{N_x + \frac{1}{2}} = L, \quad -V_c = v_{\frac{1}{2}} < v_{\frac{3}{2}} < \dots < v_{N_v + \frac{1}{2}} = V_c,$$

where V_c is chosen appropriately large to guarantee $f(x, v, t) = 0$ for $|v| \geq V_c$. This is a reasonable assumption, because of the well-posedness of the one-dimensional Vlasov-Poisson system as indicated in [21]. The grid is defined as

$$I_{i,j} = [x_{i-\frac{1}{2}}, x_{i+\frac{1}{2}}] \times [v_{j-\frac{1}{2}}, v_{j+\frac{1}{2}}], \\ J_i = [x_{i-1/2}, x_{i+1/2}], \quad K_j = [v_{j-1/2}, v_{j+1/2}], \quad i = 1, \dots, N_x, \quad j = 1, \dots, N_v,$$

where $x_i = \frac{1}{2}(x_{i-\frac{1}{2}} + x_{i+\frac{1}{2}})$ and $v_j = \frac{1}{2}(v_{j-1/2} + v_{j+1/2})$ are center points of the cells.

We will make use of several approximation spaces. For the x -domain, we consider the piecewise polynomial space of functions $\xi : \Omega_x \rightarrow \mathbb{R}$,

$$Z_h^l = \{\xi : \xi|_{J_i} \in P^l(J_i), \quad i = 1, \dots, N_x\},$$

where $P^l(J_i)$ is the space of polynomials in one dimension of degree up to l . For the (x, v) space, we consider two approximation spaces of functions $\phi, \varphi : \Omega \rightarrow \mathbb{R}$,

$$V_h^l = \{\phi : \phi|_{I_{i,j}} \in \mathbb{Q}^l(I_{i,j}), \quad i = 1, \dots, N_x, \quad j = 1, \dots, N_v\}$$

and

$$W_h^l = \{\varphi : \varphi|_{I_{i,j}} \in \mathbb{P}^l(I_{i,j}), \quad i = 1, \dots, N_x, \quad j = 1, \dots, N_v\},$$

where $\mathbb{Q}^l(I_{i,j}) = P^l(J_i) \otimes P^l(K_j) = \text{span}\{x^{l_1} v^{l_2}, \forall 0 \leq l_1 \leq l, 0 \leq l_2 \leq l\}$ denotes all polynomials of degree at most l in x and v on $I_{i,j}$, and $\mathbb{P}^l(I_{i,j}) = \text{span}\{x^{l_1} v^{l_2}, \forall 0 \leq l_1 + l_2 \leq l, l_1 \geq 0, l_2 \geq 0\}$. These two spaces are widely considered in the DG literature for multi-dimensional problems. A simple calculation shows that the number of degrees of freedom of $\mathbb{Q}^l(I_{i,j})$ is $(l+1)^2$. For $l \geq 1$ this is larger than the number of degrees of freedom of $\mathbb{P}^l(I_{i,j})$, which is $(l+1)(l+2)/2$.

First we describe the RKDG scheme for the linear Vlasov equation. We seek $f_h(x, t) \in V_h^l$ (or W_h^l), such that

$$\begin{aligned} \int_{I_{i,j}} (f_h)_t \varphi_h \, dx dv - \int_{I_{i,j}} v f_h (\varphi_h)_x \, dx dv + \int_{K_j} (\widehat{v f_h \varphi_h^-})_{i+\frac{1}{2}, v} \, dv \\ - \int_{K_j} (\widehat{v f_h \varphi_h^+})_{i-\frac{1}{2}, v} \, dv = \int_{I_{i,j}} E_h f'_{eq} \varphi_h \, dx dv \end{aligned} \quad (4)$$

holds for any test function $\varphi_h(x, t) \in V_h^l$ (or W_h^l). Here and below, we use the following notations: E_h is the discrete electric field, which is to be computed from Poisson's equation, $(\varphi_h)_{i+1/2, v}^\pm = \lim_{\epsilon \rightarrow 0} \varphi_h(x_{i+1/2} \pm \epsilon, v)$, $(\varphi_h)_{x, j+1/2}^\pm = \lim_{\epsilon \rightarrow 0} \varphi_h(x, v_{j+1/2} \pm \epsilon)$, and \widehat{vf}_h is a numerical flux. We can assume that in each K_j , v has a single sign by properly partitioning the mesh. Then, the upwind flux is defined as

$$\widehat{vf}_h = \begin{cases} vf_h^- & \text{if } v \geq 0 \text{ in } K_j \\ vf_h^+ & \text{if } v < 0 \text{ in } K_j \end{cases}. \quad (5)$$

The scheme for the nonlinear Vlasov equation is similar. We seek $f_h(x, t) \in V_h^l$ (or W_h^l), such that

$$\begin{aligned} & \int_{I_{i,j}} (f_h)_t \varphi_h dx dv - \int_{I_{i,j}} vf_h(\varphi_h)_x dx dv + \int_{K_j} (\widehat{vf}_h \varphi_h^-)_{i+\frac{1}{2}, v} dv - \int_{K_j} (\widehat{vf}_h \varphi_h^+)_{i-\frac{1}{2}, v} dv \\ & + \int_{I_{i,j}} E_h f_h(\varphi_h)_v dx dv - \int_{J_i} (\widehat{E_h f_h} \varphi_h^-)_{x, j+\frac{1}{2}} dx + \int_{J_i} (\widehat{E_h f_h} \varphi_h^+)_{x, j-\frac{1}{2}} dx = 0 \end{aligned} \quad (6)$$

holds for any test function $\varphi_h(x, t) \in V_h^l$ (or W_h^l). The upwind flux for \widehat{vf}_h has been defined in (5) and the new flux needed for the nonlinear case is given by

$$\widehat{E_h f_h} = \begin{cases} E_h f_h^- & \text{if } \int_{J_i} E_h dx \leq 0 \\ E_h f_h^+ & \text{if } \int_{J_i} E_h dx > 0 \end{cases}. \quad (7)$$

The above descriptions coupled with a suitable time discretization scheme, such as the TVD Runge-Kutta method [44], completes the RKDG methods. For example, suppose the semi-discrete schemes in (4) and (6) are written in the compact form

$$\int_{I_{i,j}} (f_h)_t \varphi_h dx dv = \mathcal{H}_{i,j}(f_h, E_h, \varphi_h)$$

where for the linear Vlasov of (4)

$$\begin{aligned} \mathcal{H}_{i,j}^{lin}(f_h, E_h, \varphi_h) &= \int_{I_{i,j}} vf_h(\varphi_h)_x dx dv - \int_{K_j} (\widehat{vf}_h \varphi_h^-)_{i+\frac{1}{2}, v} dv \\ &+ \int_{K_j} (\widehat{vf}_h \varphi_h^+)_{i-\frac{1}{2}, v} dv + \int_{I_{i,j}} E_h f'_{eq} \varphi_h dx dv, \end{aligned}$$

while for the nonlinear Vlasov of (6)

$$\begin{aligned} \mathcal{H}_{i,j}^{nonlin}(f_h, E_h, \varphi_h) &= \int_{I_{i,j}} vf_h(\varphi_h)_x dx dv - \int_{K_j} (\widehat{vf}_h \varphi_h^-)_{i+\frac{1}{2}, v} dv + \int_{K_j} (\widehat{vf}_h \varphi_h^+)_{i-\frac{1}{2}, v} dv \\ &- \int_{I_{i,j}} E_h f_h(\varphi_h)_v dx dv + \int_{J_i} (\widehat{E_h f_h} \varphi_h^-)_{x, j+\frac{1}{2}} dx - \int_{J_i} (\widehat{E_h f_h} \varphi_h^+)_{x, j-\frac{1}{2}} dx. \end{aligned}$$

The third order TVD-RK method implements the following procedure for going from t^n to t^{n+1} :

$$\begin{aligned} \int_{I_{i,j}} f_h^{(1)} \varphi_h dx dv &= \int_{I_{i,j}} f_h^n \varphi_h dx dv + \Delta t \mathcal{H}_{i,j}(f_h^n, E_h^n, \varphi_h), \\ \int_{I_{i,j}} f_h^{(2)} \varphi_h dx dv &= \frac{3}{4} \int_{I_{i,j}} f_h^n \varphi_h dx dv + \frac{1}{4} \int_{I_{i,j}} f_h^{(1)} \varphi_h dx dv + \frac{\Delta t}{4} \mathcal{H}_{i,j}(f_h^{(1)}, E_h^{(1)}, \varphi_h), \\ \int_{I_{i,j}} f_h^{n+1} \varphi_h dx dv &= \frac{1}{3} \int_{I_{i,j}} f_h^n \varphi_h dx dv + \frac{2}{3} \int_{I_{i,j}} f_h^{(2)} \varphi_h dx dv + \frac{2\Delta t}{3} \mathcal{H}_{i,j}(f_h^{(2)}, E_h^{(2)}, \varphi_h). \end{aligned} \quad (8)$$

Poisson's equation is used to obtain E_h^n , $E_h^{(1)}$, and $E_h^{(2)}$. Beyond periodicity, we need to enforce some additional conditions to uniquely determine Φ . For example, we can set one end of the spatial domain to ground, i.e. set $\Phi(0, t) = 0$. In the one-dimensional case, then the exact solution can be obtained if we enforce $\Phi(0) = \Phi(L)$. For the nonlinear system we obtain

$$\Phi_h = \int_0^x \int_0^s \rho_h(z, t) dz ds - \frac{x^2}{2} - C_E x,$$

where $C_E = -L/2 + \int_0^L \int_0^s \rho_h(z, t) dz ds / L$, and

$$E_h = -(\Phi_h)_x = C_E + x - \int_0^x \rho_h(z, t) dz, \quad (9)$$

while for the linear system Poisson's equation gives

$$\Phi_h = \int_0^x \int_0^s \rho_h(z, t) dz ds - C_E x,$$

where $C_E = \int_0^L \int_0^s \rho_h(z, t) dz ds / L$, and

$$E_h = -(\Phi_h)_x = C_E - \int_0^x \rho_h(z, t) dz. \quad (10)$$

From (9) and (10), we see that if $f_h \in V_h^l$ (or W_h^l), then $\rho_h = \int_{-V_c}^{V_c} f_h dv \in Z_h^l$; hence, $E_h \in Z_h^{l+1} \cap C^0$. The above approach uses the classical representation of the solution by Green's function and will be referred to as the "exact" Poisson solver. It is valid only for the one-dimensional case. For higher dimensions, a suitable elliptic solver needs to be implemented, such as those discussed in [23]. Here we use the exact solver to entirely eliminate discretization error from Poisson's equation and, thereby, spotlight the performance of the Vlasov solver.

Below we describe positivity-preserving limiters, as summarized in [54]. We only use such a limiter to enforce the positivity of f_h for the nonlinear VP system. For each of the forward Euler steps of the Runge-Kutta time discretization, the following procedures are performed:

- On each cell $I_{i,j}$, we evaluate $T_{i,j} := \min_{(x,v) \in S_{i,j}} f_h(x, v)$, where $S_{i,j} = (S_i^x \otimes \hat{S}_j^y) \cup (\hat{S}_i^x \otimes S_j^y)$, and S_i^x, S_j^y denote the $(l+1)$ Gauss quadrature points, while \hat{S}_i^x, \hat{S}_j^y denote the $(l+1)$ Gauss-Lobatto quadrature points.

- We compute $\tilde{f}_h(x, v) = \theta(f_h(x, v) - (\overline{f_h})_{i,j}) + (\overline{f_h})_{i,j}$, where $(\overline{f_h})_{i,j}$ is the cell average of f_h on $I_{i,j}$, and $\theta = \min\{1, |(\overline{f_h})_{i,j}|/|T_{i,j} - (\overline{f_h})_{i,j}|\}$. This limiter has the effect of maintaining the cell average, while “squeezing” the function to be positive at all points in $S_{i,j}$.
- Finally, we use \tilde{f}_h instead of f_h to compute the Euler forward step.

This completes the description of the numerical algorithm.

2.2 Scheme Conservation properties

In the following, we will briefly review and discuss some of the conservation properties of the above RKDG scheme for the nonlinear VP equations without the positivity-preserving limiter. Some of those results have been reported in [22] and [3].

Proposition 1 (*charge conservation*) *For both the V_h^l and W_h^l spaces,*

$$\sum_{i,j} \mathcal{H}_{i,j}^{nonlin}(f_h, E_h, 1) = \Theta(f_h, E_h, 1)$$

which implies

$$\begin{aligned} \sum_{i,j} \int_{I_{i,j}} f_h^{n+1} dx dv &= \sum_{i,j} \int_{I_{i,j}} f_h^n dx dv + \frac{2}{3} \Delta t (\Theta(f_h^{(2)}, E_h^{(2)}, 1)) \\ &\quad + \frac{1}{4} \Theta(f_h^{(1)}, E_h^{(1)}, 1) + \frac{1}{4} \Theta(f_h^n, E_h^n, 1) \end{aligned}$$

for the fully discrete scheme (8). Here,

$$\Theta(f_h, E_h, \varphi_h) = \sum_i \int_{J_i} (\widehat{E_h f_h \varphi_h})_{x, N_v + \frac{1}{2}} dx - \sum_i \int_{J_i} (\widehat{E_h f_h \varphi_h})_{x, \frac{1}{2}} dx$$

denotes the contribution from the phase space boundaries located at $v = \pm V_c$, and should be negligible if V_c is chosen large enough.

Remark: Charge conservation (or mass conservation or probability normalization as it is sometimes called) states that the total charge will be preserved on the discrete level up to approximation errors associated with the phase space boundaries. The proof is straightforward and, therefore, omitted. The same conclusion can be proven for the linearized system. The positivity preserving limiter does not destroy this property because it keeps the cell averages unchanged.

Proposition 2 (*Semi-discrete L^2 stability – enstrophy decay*) *For both the V_h^l and W_h^l spaces, $\sum_{i,j} \mathcal{H}_{i,j}^{nonlin}(f_h, E_h, f_h) \leq 0$. Hence,*

$$\frac{d}{dt} \sum_{i,j} \int_{I_{i,j}} f_h^2 dx dv \leq 0.$$

The proof, for an arbitrary field E_h , can be found in [10], Theorem 4, which applies directly here by setting the collisional form $Q_\sigma \equiv 0$ in that proof.

For the remainder of this subsection we will assume the DG solution satisfies the velocity boundary conditions $f_h(x, \pm V_c, t) = 0$. This is a reasonable assumption when V_c is large enough. In particular, this will guarantee exact charge conservation, which implies that $\int_0^L \rho_h(x, t) dx$ is constant in time t . Therefore, using the definition of E_h in (9), we can obtain periodicity in E_h , i.e, $E_h(0) = E_h(L)$. Without this assumption the propositions below contain multiple boundary terms and the proof becomes technical.

Proposition 3 (*Momentum conservation*) *Assuming $f_h(x, \pm V_c, t) = 0$, for both the V_h^l and W_h^l spaces when $l \geq 1$, $\sum_{i,j} \mathcal{H}_{i,j}^{nonlin}(f_h, E_h, v) = 0$, which implies*

$$\sum_{i,j} \int_{I_{i,j}} f_h^{n+1} v dx dv = \sum_{i,j} \int_{I_{i,j}} f_h^n v dx dv$$

for the fully discrete scheme.

Proof. Choosing $\varphi_h = v$ in (6), we have

$$\begin{aligned} \sum_{i,j} \mathcal{H}_{i,j}^{nonlin}(f_h, E_h, v) &= \sum_{i,j} \left(\int_{I_{i,j}} v f_h(v)_x dx dv - \int_{K_j} (\widehat{v f_h v})_{i+\frac{1}{2},v} dv + \int_{K_j} (\widehat{v f_h v})_{i-\frac{1}{2},v} dv \right. \\ &\quad \left. - \int_{I_{i,j}} E_h f_h dx dv + \int_{J_i} (\widehat{E_h f_h v})_{x,j+\frac{1}{2}} dx - \int_{J_i} (\widehat{E_h f_h v})_{x,j-\frac{1}{2}} dx \right) \\ &= - \sum_{i,j} \int_{I_{i,j}} E_h f_h dx dv = - \sum_i \int_{J_i} E_h \rho_h dx, \end{aligned}$$

and using the exact Poisson solver together with the periodicity of E_h and Φ_h yields the following:

$$\begin{aligned} \sum_i \int_{J_i} E_h \rho_h dx &= \sum_i \int_{J_i} E_h (\rho_h - 1) dx + \sum_i \int_{J_i} E_h dx \\ &= - \sum_i \int_{J_i} E_h (E_h)_x dx + \sum_i \int_{J_i} E_h dx \\ &= -(E_h^2(L) - E_h^2(0))/2 - \Phi(L) + \Phi(0) = 0, \end{aligned}$$

which completes the proof. \square

Remark: The above proof holds for the linearized system as well. Note, however, it relies on the use of the exact Poisson solver. For a full numerical DG Poisson solver, such as that developed in [23] for the discretization Poisson equation, exact momentum conservation remains true, as was proven in [22] by means of the DFUG method developed there for dealing with the discretized Poisson equation. However, the positivity-preserving limiter we use here will destroy this property because it was not designed to conserve the numerical momentum.

Proposition 4 (*Semi-discrete total energy equality*) Assuming $f_h(x, \pm V_c, t) = 0$, for both the V_h^l and W_h^l spaces when $l \geq 2$,

$$\frac{d}{dt} \left(\frac{1}{2} \sum_{i,j} \int_{I_{i,j}} f_h v^2 dx dv + \frac{1}{2} \sum_i \int_{J_i} E_h^2(x) dx \right) = A(f_h, \Phi_h) = A(f_h - f, \Phi_h - P(\Phi_h)),$$

where the operator $A(w, u) := \sum_{i,j} \int_{I_{i,j}} (wu_{xv} - (w)_t u) dx dv$, and P is any projection such that $P(\Phi_h) \in Z_h^l$ and $P(\Phi_h) = \Phi_h$ at $x_{i+1/2}$, for $i = 0, 1, \dots, N_x$.

Proof. Choosing $\varphi_h = v^2/2$ in (6) yields

$$\frac{d}{dt} \sum_{i,j} \frac{1}{2} \int_{I_{i,j}} f_h v^2 dx dv + \sum_{i,j} \int_{I_{i,j}} E_h f_h v dx dv = 0$$

and

$$\begin{aligned} \frac{d}{dt} \sum_i \frac{1}{2} \int_{J_i} E_h^2(x) dx &= \sum_i \int_{J_i} E_h (E_h)_t dx = - \sum_i \int_{J_i} (\Phi_h)_x (E_h)_t dx \\ &= \sum_i \int_{J_i} \Phi_h (E_h)_{xt} dx = \sum_i \int_{J_i} \Phi_h (1 - \rho_h)_t dx \\ &= - \sum_i \int_{J_i} \Phi_h (\rho_h)_t dx = - \sum_{i,j} \int_{I_{i,j}} \Phi_h (f_h)_t dx dv, \end{aligned}$$

where in the second line, we have used the periodicity and continuity of E_h and Φ_h . Therefore, we have proven that

$$\frac{d}{dt} \left(\frac{1}{2} \sum_{i,j} \int_{I_{i,j}} f_h v^2 dx dv + \frac{1}{2} \sum_i \int_{J_i} E_h^2(x) dx \right) = A(f_h, \Phi_h).$$

On the other hand, upon choosing $\varphi_h = P(\Phi_h)$ in (6) and using the periodicity and continuity of $P(\Phi_h)$, we can verify that $A(f_h, P(\Phi_h)) = 0$. The exact solution f obviously satisfies $A(f, \Phi_h - P(\Phi_h)) = 0$ from the continuity and periodicity of $\Phi_h - P(\Phi_h)$, and therefore we are done. \square

The above proof indicates that the variation in the total energy will be related to the error of the solution, $f_h - f$, together with the projection error, $\Phi_h - P(\Phi_h)$. In [22, 23], error estimates for DG schemes with NIPG methods for the Poisson equations are provided for multiple dimensions. In [3], optimal accuracy of order $l + 1$ for the semi-discrete scheme with \mathbb{Q}^l spaces has been proven under certain regularity assumptions. We remark that in [3] conservation of the total numerical energy is proven when the Poisson equation is solved by a local DG method with a special flux. Unfortunately, no numerical simulations of linear Landau damping or of the nonlinear VP system, such as those done in [23] or in Section 4 of this present manuscript, have been performed up to this date by the scheme proposed in [3], so a comparison is not possible.

3 On recurrence

In this section we study recurrence, a numerical phenomenon that is known to occur in simulations of Vlasov-like equations. Its study is important because it provides information about the numerical accuracy of a scheme. Recurrence was observed in the semi-Lagrangian scheme of Cheng and Knorr [8], where a simple argument for its occurrence was provided. In this section, we carry out a detailed study of recurrence for the DG method.

We study recurrence of our algorithm applied to the linear advection equation $f_t + v f_x = 0$ on $[0, L = 2\pi/k] \times [-V_c, V_c]$, since it is tractable and contains the basic recurrence mechanism; results for the full Vlasov system tend to be quite similar. The initial condition we consider is $f_0(x, v) = A \cos(kx) f_{eq}(v)$, and the equilibrium distribution $f_{eq}(v)$ is taken to be either the Maxwellian or Lorentzian distribution, viz.

$$f_M = \frac{1}{\sqrt{2\pi}} e^{-v^2/2} \quad \text{or} \quad f_L = \frac{1}{\pi} \frac{1}{v^2 + 1}.$$

For the Maxwellian equilibrium, f_M , we take $V_c = 5$, and for the Lorentzian equilibrium, f_L , we take $V_c = 30$.

The exact solution for the advection equation is $f(t, x, v) = f_0(x - vt, v)$. Hence, a simple calculation shows $\rho(x, t) = A \cos(kx) e^{-k^2 t^2/2}$ for the Maxwellian distribution; similarly, for the Lorentzian, $\rho(x, t) = A \cos(kx) e^{-kt}$. Thus, we see how the density for each case should decay to zero. The failure of decay and the occurrence of recurrence noted for the semi-Lagrangian scheme of [8] stems from the finite resolution in the velocity space and, indeed, the recurrence time depends on the mesh size in v .

To be specific, we repeat the definition of DG scheme for this equation, which amounts to (6) with E_h set to zero: we find $f_h(x, t) \in V_h^k$ (or W_h^k), such that

$$\int_{I_{i,j}} (f_h)_t \varphi_h dx dv - \int_{I_{i,j}} v f_h (\varphi_h)_x dx dv + \int_{K_j} (\widehat{v f_h \varphi_h^-})_{i+\frac{1}{2},v} dv - \int_{K_j} (\widehat{v f_h \varphi_h^+})_{i-\frac{1}{2},v} dv = 0 \quad (11)$$

holds for any test function $\varphi_h(x, t) \in V_h^k$ (or W_h^k). Again $\widehat{v f_h}$ is the upwind numerical flux of (5). In the analysis below, we always assume time to be continuous, because recurrence is mainly a phenomenon that comes from the spatial and velocity discretization.

3.1 The case of $l = 0$

For the piecewise constant case, the DG method is equivalent to a simple first order finite volume scheme and we can derive rigorously the behavior for ρ . Suppose we define $f_h = f_{ij}$ on cell I_{ij} , and assume uniform grids in both directions. Moreover, we assume N_v to be even for simplicity. With this assumption, the location of the cell center is $v_j = (j - \frac{N_v+1}{2})\Delta v$. Now (11) simply becomes

$$\begin{aligned} \frac{df_{ij}}{dt} + v_j \frac{f_{ij} - f_{i-1,j}}{\Delta x} &= 0 \quad \text{if } v_j \geq 0, \\ \frac{df_{ij}}{dt} + v_j \frac{f_{i+1,j} - f_{ij}}{\Delta x} &= 0 \quad \text{if } v_j < 0. \end{aligned} \quad (12)$$

The initial condition chosen is clearly equivalent to $f_{ij}(0) = \text{Re}(Ae^{ikx_i} f_{eq}(v_j))$. We prove that the scheme above gives

$$f_{ij}(t) = \text{Re}(Ae^{ikx_i + s_j t} f_{eq}(v_j)) \quad (13)$$

where s_j is given in (14) below.

Upon plugging (13) into (12), we have

$$s_j f_{ij} + v_j \frac{1 - e^{-ik\Delta x}}{\Delta x} f_{ij} = 0 \quad \text{if } v_j \geq 0$$

$$s_j f_{ij} + v_j \frac{e^{ik\Delta x} - 1}{\Delta x} f_{ij} = 0 \quad \text{if } v_j < 0.$$

Hence,

$$s_j = \begin{cases} -v_j \frac{1 - e^{-ik\Delta x}}{\Delta x} = v_j \frac{\cos(k\Delta x) - 1}{\Delta x} - v_j \frac{\sin(k\Delta x)}{\Delta x} i & \text{if } v_j \geq 0 \\ -v_j \frac{e^{ik\Delta x} - 1}{\Delta x} = -v_j \frac{\cos(k\Delta x) - 1}{\Delta x} - v_j \frac{\sin(k\Delta x)}{\Delta x} i & \text{if } v_j < 0, \end{cases}$$

which can be summarized as

$$s_j = |v_j| \frac{\cos(k\Delta x) - 1}{\Delta x} - v_j \frac{\sin(k\Delta x)}{\Delta x} i. \quad (14)$$

Therefore, the real part of s_j is always negative, this means the magnitude of f_{ij} will always damp, but because of the j -dependence it does so at different rates for different cells. Since the density

$$\rho(x_i) = \sum_j f_{ij} \Delta v = \text{Re} \left(\sum_j A e^{ikx_i + s_j t} f_{eq}(v_j) \right) \Delta v,$$

the density will damp at a rate between $\frac{\Delta v}{2} \frac{\cos(k\Delta x) - 1}{\Delta x}$ and $\frac{V_c - \Delta v}{2} \frac{\cos(k\Delta x) - 1}{\Delta x}$. Another important fact is that recurring local maxima of the density will have a period T_R that satisfies $\frac{\Delta v}{2} \frac{\sin(k\Delta x)}{\Delta x} T_R = \pi$. If we define $k' = \frac{\sin(k\Delta x)}{\Delta x}$, then $T_R = \frac{2\pi}{k' \Delta v}$. When $\Delta x \rightarrow 0$, $k' \rightarrow k$, and this coincides with the recurrence time obtained in [8].

Next we compare the above theoretical prediction with numerical results. In all of the calculations below, we take $A = 1$, $k = 0.5$ and the mesh size to be 40×40 . In Figure 1, we display results for numerical runs using piecewise constant polynomials and time discretization using TVD-RK3. (We use the third order method to minimize the time discretization error.) We plot $\rho_{max}(t) = \max_x \rho(x, t)$ in Figure 1. First, we notice the pattern of ρ_{max} has the expected periodic structure with damping for both Maxwellian and Lorentzian equilibria. For the Maxwellian distribution, a simple calculation yields $T_R = 50.47$. Similarly, with the formulas above, the smallest damping rate is -0.49×10^{-2} , while the biggest is -9.3×10^{-2} . For the Lorentzian distribution, $T_R = 8.41$, and the smallest damping rate is -2.94×10^{-2} , while the biggest is -5.58×10^{-1} . From Figure 1, by using the second to the fourth peak, the actual computed value of T_R for Maxwellian is 50.32 and the damping rate is -1.02×10^{-2} ; while for Lorentzian, from the second to the tenth peak, T_R is 8.40 and the computed damping rate is -3.19×10^{-2} . These numbers agree well with the theoretical prediction.

In conclusion, our analysis explains the behavior of the first order DG solution. At $t = T_R$, the numerical density obtains a local maximum; hence, clearly at this time the numerical

solution can no longer be trusted. The numerical decay deviates from the theoretical decay well before $t = T_R$. To achieve a larger T_R , according to the formula, we can refine Δv . On the other hand, refining Δx will not change T_R by much.

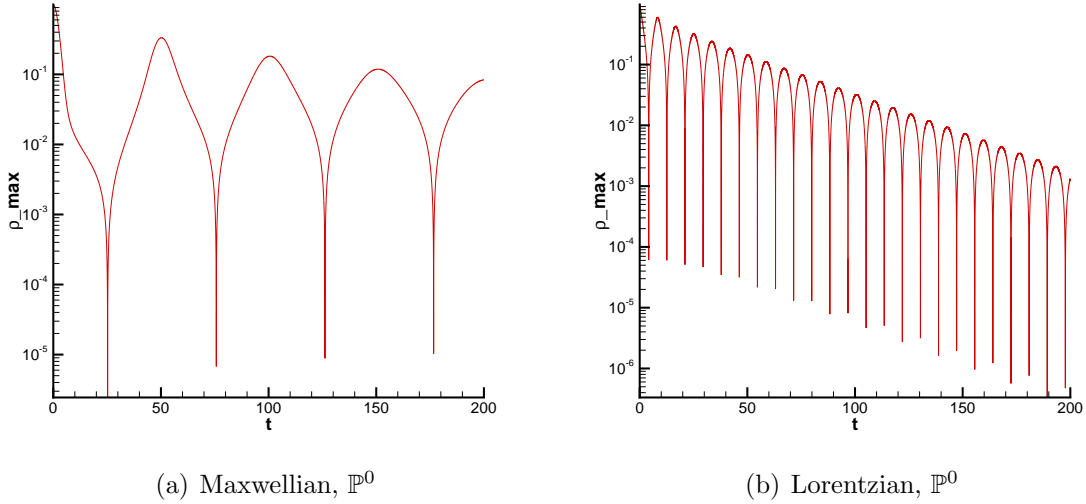


Figure 1: Computations of the advection equation for piecewise constant polynomials showing local maxima of the density ρ_{max} as a function of time. The mesh is 40×40 with $\Delta x = \pi/10$. For the Maxwellian equilibrium $\Delta v = 1/4$, while for the Lorentzian equilibrium $\Delta v = 3/2$.

Remark: Using the same methodology, it is easy to perform a similar analysis for any type of finite difference method. The real part of s_j will be negative if there is numerical dissipation, and the imaginary part will always approximate $v_j k$ due to the differential operator $v \frac{\partial}{\partial x}$. This means that for such schemes, the recurrence time T_R will always be close to $\frac{2\pi}{k\Delta v}$.

3.2 Higher order polynomials

In this subsection, we consider higher order polynomials. For the V_h^1 space, it takes four point values in each cell to represent a \mathbb{Q}^1 polynomial. This technique was developed in [51] for analyzing piecewise linear DG solutions in one dimension. As in Section 3.1, we use a uniform mesh, i.e. $\Delta x_i \equiv \Delta x$ and $\Delta v_j \equiv \Delta v$. Without loss of generality, we consider (11) for the case of $v \geq 0$ only, then $\widehat{v}f_h = vf_h^-$, which means we only consider cells $I_{i,j}$ with $j \geq \frac{N_v}{2} + 1$.

In each computational cell $I_{i,j}$, we can always use the following form to represent f_h :

$$f_h = f_{i-\frac{1}{4},j+\frac{1}{4}} \chi_1(x, v) + f_{i-\frac{1}{4},j-\frac{1}{4}} \chi_2(x, v) + f_{i+\frac{1}{4},j+\frac{1}{4}} \chi_3(x, v) + f_{i+\frac{1}{4},j-\frac{1}{4}} \chi_4(x, v),$$

where

$$\begin{aligned}
\chi_1(x, v) &= -4 \left(\frac{x - x_i}{\Delta x_i} - \frac{1}{4} \right) \left(\frac{v - v_j}{\Delta v_j} + \frac{1}{4} \right) \\
\chi_2(x, v) &= 4 \left(\frac{x - x_i}{\Delta x_i} - \frac{1}{4} \right) \left(\frac{v - v_j}{\Delta v_j} - \frac{1}{4} \right) \\
\chi_3(x, v) &= 4 \left(\frac{x - x_i}{\Delta x_i} + \frac{1}{4} \right) \left(\frac{v - v_j}{\Delta v_j} + \frac{1}{4} \right) \\
\chi_4(x, v) &= -4 \left(\frac{x - x_i}{\Delta x_i} + \frac{1}{4} \right) \left(\frac{v - v_j}{\Delta v_j} - \frac{1}{4} \right)
\end{aligned}$$

are the basis functions in \mathbb{Q}^1 and $f_{i\pm 1/4, j\pm 1/4} = f_h(x_{i\pm 1/4}, v_{j\pm 1/4})$ are the point values. By choosing the test function in (11) to be $\varphi_h = \chi_\ell$, $\ell = 1, 2, 3, 4$, we obtain four relations. Letting $f_{ij} = (f_{i-1/4, j+1/4}, f_{i-1/4, j-1/4}, f_{i+1/4, j+1/4}, f_{i+1/4, j-1/4})^T$, then corresponding to each of the four terms in (11), we have

$$M \frac{df_{ij}}{dt} - B f_{ij} + C f_{i,j} - D f_{i-1,j} = 0,$$

where

$$\begin{aligned}
M &= \frac{\Delta x \Delta v}{144} \begin{pmatrix} 49 & -7 & -7 & 1 \\ -7 & 49 & 1 & -7 \\ -7 & 1 & 49 & -7 \\ 1 & -7 & -7 & 49 \end{pmatrix}, \\
B &= \frac{\Delta v}{12} \begin{pmatrix} -(2\Delta v + 7v_j) & v_j & -(2\Delta v + 7v_j) & v_j \\ v_j & 2\Delta v - 7v_j & v_j & 2\Delta v - 7v_j \\ 2\Delta v + 7v_j & -v_j & 2\Delta v + 7v_j & -v_j \\ -v_j & -2\Delta v + 7v_j & -v_j & -2\Delta v + 7v_j \end{pmatrix}, \\
C &= \frac{\Delta v}{48} \begin{pmatrix} 2\Delta v + 7v_j & -v_j & -(6\Delta v + 21v_j) & 3v_j \\ -v_j & -2\Delta v + 7v_j & 3v_j & 6\Delta v - 21v_j \\ -6\Delta v - 21v_j & 3v_j & 18\Delta v + 63v_j & -9v_j \\ 3v_j & 6\Delta v - 21v_j & -9v_j & -18\Delta v + 63v_j \end{pmatrix},
\end{aligned}$$

and

$$D = \frac{\Delta v}{48} \begin{pmatrix} -6\Delta v - 21v_j & 3v_j & 18\Delta v + 63v_j & -9v_j \\ 3v_j & 6\Delta v - 21v_j & -9v_j & -18\Delta v + 63v_j \\ 2\Delta v + 7v_j & -v_j & -6\Delta v - 21v_j & 3v_j \\ -v_j & -2\Delta v + 7v_j & 3v_j & 6\Delta v - 21v_j \end{pmatrix}.$$

After simple algebraic manipulation, we obtain

$$\frac{df_{ij}}{dt} = \frac{\Delta v}{\Delta x} (S_m f_{ij} + T_m f_{i-1,j}),$$

where

$$S_m = \begin{pmatrix} -\frac{49}{96} - \frac{7m}{8} & \frac{7}{96} & -\frac{7}{32} - \frac{3m}{8} & \frac{1}{32} \\ -\frac{7}{96} & \frac{49}{96} - \frac{7m}{8} & -\frac{1}{32} & \frac{7}{32} - \frac{3m}{8} \\ \frac{77}{96} + \frac{11m}{8} & -\frac{11}{96} & -\frac{21}{32} - \frac{9m}{8} & \frac{3}{32} \\ \frac{11}{96} & -\frac{77}{96} + \frac{m}{8} & -\frac{3}{32} & \frac{21}{32} - \frac{9m}{8} \end{pmatrix},$$

$$T_m = \begin{pmatrix} -\frac{35}{96} - \frac{5m}{8} & \frac{5}{96} & \frac{35}{32} + \frac{15m}{8} & -\frac{5}{32} \\ -\frac{5}{96} & \frac{35}{96} - \frac{5m}{8} & \frac{5}{32} & -\frac{35}{32} + \frac{15m}{8} \\ \frac{7}{96} + \frac{m}{8} & -\frac{1}{96} & -\frac{7}{32} - \frac{3m}{8} & \frac{1}{32} \\ \frac{1}{96} & -\frac{7}{96} + \frac{m}{8} & -\frac{1}{32} & \frac{7}{32} - \frac{3m}{8} \end{pmatrix},$$

and $m = 2j - N_v - 1 = 1, 3, 5, \dots$ are positive and odd integers. Therefore, the amplification matrix is given by

$$G_j = \frac{\Delta v}{\Delta x} (S_m + T_m e^{-ik\Delta x}).$$

With the initial condition $f_{ij}(0) = \text{Re}(Ae^{ikx_i}\Upsilon)$, where

$$\Upsilon = \left(e^{-ik\Delta x/4} f_{eq}(v_{j+\frac{1}{4}}), e^{-ik\Delta x/4} f_{eq}(v_{j-\frac{1}{4}}), e^{ik\Delta x/4} f_{eq}(v_{j+\frac{1}{4}}), e^{ik\Delta x/4} f_{eq}(v_{j-\frac{1}{4}}) \right)^T,$$

it is clear that the general expression for the numerical solution is

$$f_{ij}(t) = \text{Re} \left(e^{ikx_i} \sum_{\alpha=1}^4 a_\alpha V_\alpha e^{\eta_\alpha t} \right).$$

Here η_α are the eigenvalues of G_j with V_α the corresponding eigenvectors, a_α are constants such that $f_{ij}(0) = \Upsilon$, and all these quantities are dependent on j (or equivalently $m = 2j - N_v - 1$). The collective behaviors of the eigenvalues η_α will influence the behavior of the density as a function of time. We focus on the matrix $\Lambda_m = S_m + T_m e^{-ik\Delta x}$, which with some algebraic manipulation can be seen to have the form

$$\Lambda_m = W \otimes V,$$

where W and V are the following 2×2 matrices:

$$W = \begin{pmatrix} -3m - \frac{7}{4} & \frac{1}{4} \\ -\frac{1}{4} & -3m + \frac{7}{4} \end{pmatrix},$$

$$V = \begin{pmatrix} \frac{1}{2} + \frac{5}{24}\hat{i} & -\frac{1}{2} - \frac{5}{8}\hat{i} \\ -\frac{1}{2} - \frac{1}{24}\hat{i} & \frac{1}{2} + \frac{1}{8}\hat{i} \end{pmatrix},$$

and $\hat{i} = e^{-ik\Delta x} - 1 = -ik\Delta x + O(\Delta x^2)$. This nice structure is due to the tensor product formulations of the mesh and the space \mathbb{Q}^l . We compute the eigenvalues of the matrix V , obtaining $\lambda_1 = (3 + \hat{i} - \sqrt{9 + 12\hat{i} + \hat{i}^2})/6 = \frac{1}{6}ik\Delta x - \frac{1}{12}k^2\Delta x^2 + O(\Delta x^3)$ and $\lambda_2 = (3 + \hat{i} + \sqrt{9 + 12\hat{i} + \hat{i}^2})/6 = 1 - \frac{1}{2}ik\Delta x + O(\Delta x^2)$, and the eigenvalues of W , obtaining $-3m \pm \sqrt{3}$. Hence, by simple linear algebra, the four eigenvalues of the matrix Λ_m are obtained

$$\begin{pmatrix} \xi_1 = (-3m - \sqrt{3})\lambda_2 \\ \xi_2 = (-3m + \sqrt{3})\lambda_2 \\ \xi_3 = (-3m - \sqrt{3})\lambda_1 \\ \xi_4 = (-3m + \sqrt{3})\lambda_1 \end{pmatrix}.$$

It is easy to show that the eigenvectors corresponding to these eigenvalues are independent of m , since the eigenvectors of V and W are independent of m . We conclude that the eigenvalues of G_j are

$$\begin{pmatrix} \eta_1 = (-3m - \sqrt{3})\lambda_2\Delta v/\Delta x \\ \eta_2 = (-3m + \sqrt{3})\lambda_2\Delta v/\Delta x \\ \eta_3 = (-3m - \sqrt{3})\lambda_1\Delta v/\Delta x \\ \eta_4 = (-3m + \sqrt{3})\lambda_1\Delta v/\Delta x \end{pmatrix},$$

and therefore,

$$\begin{aligned} \sum_{\alpha=1}^4 a_\alpha V_\alpha e^{\eta_\alpha t} &= e^{-3m(\lambda_2\Delta v/\Delta x)t} \left(a_1 V_1 e^{-\sqrt{3}(\lambda_2\Delta v/\Delta x)t} + a_2 V_2 e^{\sqrt{3}(\lambda_2\Delta v/\Delta x)t} \right) \\ &\quad + e^{-3m(\lambda_1\Delta v/\Delta x)t} \left(a_3 V_3 e^{-\sqrt{3}(\lambda_1\Delta v/\Delta x)t} + a_4 V_4 e^{\sqrt{3}(\lambda_1\Delta v/\Delta x)t} \right). \end{aligned}$$

Since η_1 and η_2 have nontrivial negative real parts, the damping for those two modes will be strong. Consequently, the main behavior of the density will be dominated by the eigenmodes of η_3 and η_4 . Recall

$$\rho(x_{i\pm\frac{1}{4}}, t) = \sum_j \int_{I_j} f_h(x_{i\pm\frac{1}{4}}, v, t) dv = \sum_j (f_{i\pm\frac{1}{4}, j+\frac{1}{4}} + f_{i\pm\frac{1}{4}, j-\frac{1}{4}}) \Delta v,$$

and, therefore, the behavior of $\rho(x_{i\pm 1/4}, t)$ is dominated by

$$\sum_m e^{-3m(\lambda_1\Delta v/\Delta x)t} \left(c_3 e^{-\sqrt{3}(\lambda_1\Delta v/\Delta x)t} + c_4 e^{\sqrt{3}(\lambda_1\Delta v/\Delta x)t} \right),$$

where c_3 and c_4 are constants that do not depend on m . Since $\lambda_1 = \frac{1}{6}ik\Delta x - \frac{1}{12}k^2\Delta x^2 + O(\Delta x^3)$, we have $-3m(\lambda_1\Delta v/\Delta x) = -\frac{k\Delta v}{2}mi - \frac{m\Delta v\Delta x k^2}{4} + O(\Delta v\Delta x^2)$. Hence, with an argument similar to that of Section 3.1 for the piecewise constant case, when $t \approx T_R = \frac{2\pi}{k\Delta v}$ the imaginary parts of all modes will return to $m\pi i$, and this will correspond to a local maximum of ρ_{max} as a function of time. The remaining term, $c e^{-\sqrt{3}ik\Delta v/6t} + d e^{\sqrt{3}ik\Delta v/6t}$, corresponds to the envelope of the wave, and the negative real part of the eigenvalues indicates numerical dissipation.

In Figure 2, we plot the evolution of ρ_{max} as a function of time for the \mathbb{Q}^1 and \mathbb{Q}^2 spaces. From Figures 2(a) and 2(b), we observe the behavior predicted by our analysis for the \mathbb{Q}^1 elements. From Figures 2(c) and 2(d), we find that the solutions using the \mathbb{Q}^2 polynomials share similar structures, except that small oscillations can be observed for the Maxwellian case. Also we note that the \mathbb{Q}^2 discretizations can follow the exact solutions longer in time, in the sense that the minimum value achieved before ρ_{max} starts to deviate from the exact solution is on the order of 10^{-6} compared to 10^{-4} in the \mathbb{Q}^1 case. This is expected due to the higher order accuracy of the scheme. For the \mathbb{Q}^2 polynomials, we deduce that the amplification matrix G is a 9×9 matrix. Thus, for this case there, there will be nine eigenvalues and more modes than for the \mathbb{Q}^1 space. In Table 1, we verify the recurrence time T_R numerically; good agreement between the predicted values and the observed values are seen.

Note, the trace $Tr(S_m) = -4m, m = 1, 3, 5 \dots$, while a similar calculation for cells when $v < 0$ yields $Tr(S_m) = 4m, m = 1, 3, 5 \dots$. Therefore, we conclude that our semi-discrete

Table 1: The location of local maxima of the density ρ_{max} compared with the predicted recurrence time T_R . The T_R values for the Maxwellian equilibrium are computed using the average of the first three peaks, while for the Lorentzian they are computed using the average of the first seven peaks.

	Predicted $T_R = \frac{2\pi}{k\Delta v}$	Numerical value of \mathbb{Q}^1	Numerical value of \mathbb{Q}^2
Maxwellian	50.26548245743669	50.265482457450	50.265482457450
Lorentzian	8.37758040957278	8.37787960887962	8.37787960887760

algorithm has an incompressible vector field and thus possesses a version of Liouville’s theorem on conservation of phase space volume. Liouville’s theorem for finite difference and Fourier discretization of fluid and plasma equations is well known and has been used in statistical theories of turbulence (see e.g. [40, 31, 29, 26]). We also note that we have performed the analysis for the semi-discrete DG schemes. For fully discrete RKDG schemes, one could use a similar method, as proposed in [57] for the wave equation, to write the fully discrete amplification matrices, but we do not pursue this in this paper.

We close this section with a few comments. An analysis similar to that of this section for \mathbb{P}^1 elements yields a 3×3 matrix; however, this basis does not yield the nice form possessed by \mathbb{Q}^1 because of the loss of the tensor structure. Figure 3 shows the temporal behavior of ρ_{max} using the \mathbb{P}^l elements. Observe that, although the local maxima still are located near $T_R = \frac{2\pi}{k\Delta v}$, there appear to be several small local maxima instead of one main maximum, and overall the long time dissipation seems to be stronger than that for \mathbb{Q}^l . We also noted that the \mathbb{P}^2 basis follow the exact solution longer than \mathbb{P}^l , but shorter than \mathbb{Q}^2 cases, because for \mathbb{P}^2 elements, the minimum value that the solution achieves before it deviates from the exact solution is on the order of 10^{-4} . In summary, we conclude that increasing the polynomial order does not change T_R by much. However, higher order accuracy seems to improve the time that the numerical solution can follow the exact solution. For \mathbb{Q}^l elements, the amplification matrix can be written as a tensor product of two small matrices, and this made possible our direct analysis for the recurrence time. For \mathbb{P}^l elements, we lose this tensor structure, and the solution is more dissipative.

Finally we remark that since the linearized equation involves an operator $E f'_{eq}(v)$, where the electric field depends on the distribution function f on all cells, it is not trivial to generalize the analysis to the LVP system. However, it was proven in [38, 35] that there exists a generalization of the Hilbert transform that maps the solution of the advection equation to the solution of this LVP system, so we expect similar type of recurrence behavior for the LVP system, and this is verified by numerical calculation in Section 4.1.

4 Vlasov numerical results

Now we turn to some numerical tests of our method for both the VP and LVP systems. For the LVP system we consider the standard tests of linear and nonlinear Landau damping, which have been studied in many references in the contexts of various numerical techniques

since [8] (see [23] for an extended list), but we also consider a test that heretofore does not appear to have been done, viz., we monitor the linearized energy that is conserved by the LVP system [30, 38, 35]. Similarly, for the nonlinear VP system we consider the standard tests of nonlinear Landau damping and a symmetric version of the two-stream instability (also see [23] for references). In addition, for the VP system we consider an example that is initialized by a driving electric field, resulting in a dynamically accessible initial condition as described in [36, 37, 38], which has been observed to approach nonli near BGK [5] states that have been termed KEEN waves in Ref. [1, 25] (see also [22, 46]).

4.1 Linearized VP system

Associated with the LVP system of (3) is the well-known plasma dispersion function [20],

$$\varepsilon(k, \omega) = 1 - \frac{1}{k^2} \int_{-\infty}^{+\infty} \frac{f'_{eq}(v)}{v - \omega/k} dv, \quad (15)$$

which (with the appropriate choice of contour) will be used to benchmark the accuracy of the Landau damping rate and oscillation frequency obtained from our DG solver with choices for the various polynomial spaces. The LVP system conserves not only the total charge and momentum, but also the linear energy [30, 38, 35], which is defined as

$$H_L = -\frac{1}{2} \int_{\Omega} \frac{v f^2}{f'_{eq}} dx dv + \frac{1}{2} \int_{\Omega_x} E^2 dx. \quad (16)$$

As noted above, we monitor this quantity and check for its conservation. In addition, we monitor the shift of energy to the first term of (16) as the second decays in time in accordance with Landau damping, consistent with the discussion of [38].

Linear Landau damping

For this classical test problem, we choose the usual initial condition $f_0(x, v) = A \cos(kx) f_M(v)$, with $A = 0.01$ and $k = 0.5$. For the Maxwellian distribution function the dispersion relation becomes

$$\varepsilon(k, \omega) = 1 + \frac{1}{k^2} \left\{ 1 + \frac{\omega}{\sqrt{2}k} Z \left(\frac{\omega}{\sqrt{2}k} \right) \right\},$$

where the plasma Z -function is defined as

$$Z(z) = \frac{1}{\sqrt{\pi}} \int_{-\infty}^{\infty} e^{-t^2} \frac{dt}{t - z} = 2ie^{-z^2} \int_{-\infty}^{iz} e^{-t^2} dt.$$

From this relation, the predicted damping rate is computed to be 0.153359 and the predicted oscillation frequency to be 1.41566.

In Figures 4, we plot the evolution of the maximum of the electric field E_{max} using various polynomial spaces. In Table 2, we compare the theoretical and numerical values of damping rate and frequency as a measurement of accuracy. We see that refining the mesh always gives better approximations. The piecewise constant polynomials \mathbb{P}^0 give much larger error

Table 2: The damping rate and frequency for linear Landau damping. The numerical values are computed using the fourth to the tenth peak and the predicted value is obtained from the plasma dispersion function (15) with a Maxwellian equilibrium.

	Predicted value	Mesh	\mathbb{P}^0	\mathbb{P}^1	\mathbb{P}^2	\mathbb{Q}^1	\mathbb{Q}^2
Damping rate	0.153359	40×40	0.227489	0.153536	0.153375	0.153425	0.153379
		80×80	0.191702	0.153366	0.153363	0.15369	0.153363
Frequency	1.41566	40×40	1.38249	1.41643	1.41643	1.41643	1.41643
		80×80	1.40056	1.41576	1.41576	1.41576	1.41576

compared to higher order polynomials. While the difference between the \mathbb{P}^l and \mathbb{Q}^l spaces is not significant. Observe from Figure 4 how similar the recurrence behavior is for this LVP problem to that of the advection equation.

As for conservation properties, the charge and momentum are well conserved as predicted by Propositions 1 and 3. However, the linear energy H_L demonstrates different behaviors depending on the polynomial spaces. Figure 5 shows that H_L decays significantly for all \mathbb{P}^l spaces even upon mesh refinement. On the other hand, the \mathbb{Q}^l seems to conserve it much better. We note that \mathbb{Q}^1 conserves H_L much better than \mathbb{P}^2 , although the former is a subspace of the later.

Also, note from Figure 6 that the electrostatic energy for both choices of polynomial spaces damps at a rate given by twice the Landau damping rate. This is to be expected for the linear theory, since after integration over space the oscillatory component is removed and $E \sim \exp(-2\gamma t)$. Therefore, if the energy is conserved numerically this damped electrostatic energy must be converted into the relative kinetic energy that is represented by the first term of (16). Thus, conservation of H_L serves as a global measure of the ability of an algorithm to resolve fine scales in velocity space. That this transference must take place for the linear VP system was proven in Section IV of Ref. [38].

4.2 Nonlinear VP system

In this section, we consider the nonlinear VP system. As noted above, we benchmark the solver against three test cases: the nonlinear Landau damping, two-stream instability, and an external drive problem with dynamically accessible initial condition.

The n -th Log Fourier mode for the electric field $E(x, t)$ [23] is defined as

$$\log FM_n(t) = \log_{10} \left(\frac{1}{L} \sqrt{\left| \int_0^L E(x, t) \sin(knx) dx \right|^2 + \left| \int_0^L E(x, t) \cos(knx) dx \right|^2} \right).$$

We will use this quantity to plot data from our various runs.

Nonlinear Landau damping

For this case we choose $f_0(x, v) = f_M(v)(1 + A \cos(kx))$ with $A = 0.5$, $k = 0.5$, $L = 4\pi$, and $V_c = 6$. We implement the scheme on a 100×200 mesh and integrate up to $T = 100$ using three methods: \mathbb{P}^2 , \mathbb{P}^2 with the positivity-preserving limiter, and \mathbb{Q}^2 . In Figure 7, we plot the evolution of the first four Log Fourier modes as a function of time. All three methods give qualitatively similar results that compare well with other calculations in the literature. We observe initial damping (until $t \approx 15$), followed by exponential growth (until $t \approx 40$), and finally saturation of the modes. Note the predicted recurrence times T_R for each of the modes are as follows: for $\log FM_1$, $T_R = 209.44$; for $\log FM_2$, $T_R = 104.72$; for $\log FM_3$, $T_R = 69.81$; and for $\log FM_4$, $T_R = 52.36$. Since the bounce time is about 40, we have some confidence that the solution is resolved at least up until nonlinearity becomes important. Although, the role played by T_R for the nonlinear evolution is not clear since nonlinearity could remove the fine scales generated by linear phase mixing.

In Figure 8, we plot the conserved quantities of Section 2.2. The charge and momentum are well conserved for all methods, while the enstrophy has decayed by about 15% at $T = 100$ for all three methods. This result agrees with our analysis in Section 2. We remark that the limiter has an effect on charge conservation, due to its modification of the solution on the boundary. The total energy is conserved much better without the positivity-preserving limiter. When we use the limiter, the total energy grows by about 0.3% at $T = 100$.

Two-stream instability

For this case we choose $f_0(x, v) = f_{TS}(v)(1 + A \cos(kx))$, where $f_{TS}(v) = \frac{1}{\sqrt{2\pi}}v^2e^{-v^2/2}$, $A = 0.05$, $k = 0.5$, $L = 4\pi$, and $V_c = 6$. The mesh size we take is 100×200 . In Figure 9, we plot the evolution of conserved quantities. For this example, charge and momentum are well conserved by all methods, so are not plotted. The enstrophy decays by about 4% at $T = 100$, while the total energy is well conserved even with the limiter. The plots of the log Fourier modes show an early exponential growth followed by oscillation. Figure 10 provides evidence that the system has relaxed into a BGK mode. Here, the relation defined by the ordered pair $(\epsilon = v^2/2 + \Phi(x, T), f(x, v, t))$ is plotted at various times t . The use of this kind of plot as a diagnostic was first reported in [23] for electrostatic VP equations and later in [9] for the gravitational VP equations. Here, the evolution clearly indicates convergence to a BGK equilibrium.

Dynamically accessible excitations—KEEN waves

Motivated by experiments performed for understanding aspects of laser-plasma interaction [33], several authors have considered numerical solution of the VP system with a transitory external driving electric field (see, e.g., [1, 25]), rather than just specifying an ad hoc initial condition for f , as is usually done. Such drive generated initial conditions are examples of those proposed and discussed in [36, 37, 38], where they were termed dynamically accessible (DA) initial conditions. DA initial conditions are important because they have a Hamiltonian origin and preserve phase space constraints. Moreover, since ultimately any perturbation of charged particles within the confines of VP theory is in fact caused by an electric field, it is physically very natural to consider DA initial conditions. We consider two numerical examples and

compare our results with those of [1, 25], where the authors observed saturation to nonlinear traveling BGK-like states that they termed KEEN waves, standing for kinetic electrostatic electron nonlinear waves. We note that the calculations of [1] were duplicated in [22] and allied work was given in [46, 47].

Specifically, the system is driven by a single prescribed frequency and wavelength, where the driven Vlasov equation,

$$f_t + v f_x - (E + E_{ext}) f_v = 0,$$

is solved. Here, $E_{ext}(x, t) = A_d(t) \sin(kx - \omega t)$ is the external field, where A_d is a temporal envelope that is ramped up to a plateau and then ramped down to zero. For our two examples we consider the following two ramping profiles:

$$A_d^J(t) = \begin{cases} A_m \sin(t\pi/100) & \text{if } 0 < t < 50 \\ A_m & \text{if } 50 \leq t < 150 \\ A_m \cos((t - 150)\pi/100) & \text{if } 150 < t < 200 \\ 0 & \text{if } 200 < t < T \end{cases}, \quad (17)$$

with $A_m = 0.052$ as used in [25] and

$$A_d^A(t) = \begin{cases} A_m \frac{1}{1+e^{-40(t-10)}} & \text{if } 0 < t < 60 \\ A_m \left(1 - \frac{1}{1+e^{-40(t-110)}}\right) & \text{if } 60 \leq t < T \end{cases}, \quad (18)$$

with $A_m = 0.4$ as used in [1]. In practice, the system is initialized on $f(0, x, v) = f_M(v)$, then ramped according to (17) or (18) to prepare the DA initial condition. The system is then evolved after E_{ext} is turned off and seen to approach asymptotic states. For both cases the computational domain is of size $[0, 2\pi/k] \times [-8, 8]$, and we take $k = 0.26$ and $\omega = 0.37$.

Following [25] with the drive A_d^J of (17) with $A_m = 0.4$ we obtain for latter times a translating BKG-like state, a snapshot of which is depicted in the phase space portrait of Fig. 11. This structure moves through the spatial domain giving rise to the central periodic electric field signal, $E(0, t)$, depicted in Fig. 12. The period of this signal coincides with the propagation speed of the BKG-like state, which in agreement with [25] is about 1.35. Figure 13 shows the first four Fourier modes and indicates saturation.

Next, we increase the drive to compare with results of [1]. With the stronger drive of A_d^A with $A_m = 0.4$, the system does not approach a uniformly translating state, but approaches a structure with more complicated time dependence as seen in the phase contour plots of Fig. 14. These figures are in good agreement with those of [1].

The electric field in the middle of the spatial domain, $E(0, t)$, is plotted in Fig. 15, which shows more complicated behavior, which surprisingly heretofore has not been plotted. In the top part of this figure we see that there is regular periodic behavior at long times and from the bottom part of the figure we see that there is period-4 modulation of a basic periodic structure similar to that of Fig. 12. Closer examination of phase space plots shows that this modulation is caused by the existence of additional smaller BGK-like structures. We note,

that the existence of multiple BGK-like states is not new; for example, they were seen in the simulations of [16]. Thus, we propose that KEEN waves can be interpreted as the interaction of multiple BGK-states, which can also be interpreted as an infinite-dimensional version of Lyapunov-Moser-Weinstein periodic orbits in Hamiltonian systems (see, e.g. [39]). This will be the subject of a future publication, so we do not pursue it further here.

Finally, in Fig. 16 we see from the evolution of log Fourier modes. Prior to $t = 10$ the solution remains roughly at Maxwellian equilibrium. However, at around $t = 45$ we can observe the formation of the KEEN wave, which continues to execute the behavior of Fig. 15 well after the external field has been turned off at $t=60$. We see from this figure the effects of mesh refinement and the use of different polynomial bases, as indicated in the figure.

5 Conclusion

In this paper, we considered the RKDG method for the VP system. We focused on two common solution spaces, viz., those with \mathbb{P}^l and \mathbb{Q}^l elements. Ignoring boundary contributions, the scheme can preserve the charge and momentum, and maintain the total energy up to approximation errors when the polynomial order l is taken big enough. However, when the positivity-preserving limiter was used, some examples gave relatively large errors for the total energy. A rigorous study of numerical recurrence was performed for the \mathbb{Q}^l elements, and the eigenvalues of the amplification matrix were explicitly obtained. DG schemes of higher order were shown numerically to give a recurrence time that is close to the classical calculation $T_R = \frac{2\pi}{k\Delta v}$. The qualitative behaviors of the \mathbb{P}^l and \mathbb{Q}^l spaces were similar for most computational examples, except the linear energy H_L was much better conserved using the \mathbb{Q}^l space. The schemes were used to compute the test cases of Landau damping, the two-stream instability and the KEEN wave, and results comparable to those in the literature were obtained.

Acknowledgments

YC was supported by grant NSF DMS-1016001, IMG was supported by grants NSF DMS-0807712 and DMS-0757450, and PJM was supported by U.S. Dept. of Energy Contract # DE-FG05-80ET-53088. Also, support from the Department of Mathematics at Michigan State University and the Institute of Computational Engineering and Sciences at the University of Texas Austin are gratefully acknowledged.

References

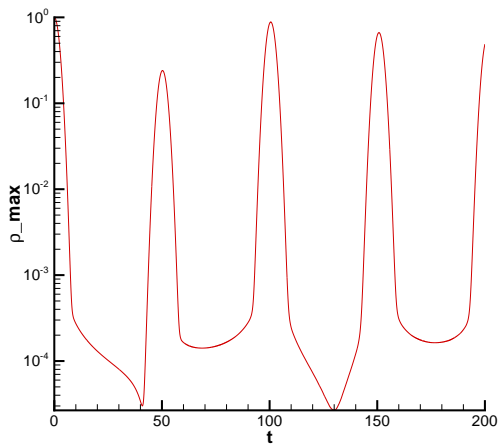
- [1] B. Afeyan, K. Won, V. Savchenko, T. Johnston, A. Ghizzo, and P. Bertrand. Kinetic Electrostatic Electron Nonlinear (KEEN) Waves and their Interactions Driven by the Ponderomotive Force of Crossing Laser Beams. *Proc. IFSA 2003*, 213, 2003.
- [2] B. Ayuso, J. A. Carrillo, and C.-W. Shu. Discontinuous Galerkin methods for the multi-dimensional Vlasov-Poisson problems. *Mathematical Models and Methods in Applied Sciences*. to appear.

- [3] B. Ayuso, J. A. Carrillo, and C.-W. Shu. Discontinuous Galerkin methods for the one-dimensional Vlasov-Poisson system. *Kinetic and Related Models*, 4:955–989, 2011.
- [4] J. Barnes and P. Hut. A hierarchical $o(n \log n)$ force-calculation algorithm. *Nature*, 324:446–449, 1986.
- [5] I. Bernstein, J. M. Greene, and M. D. Kruskal. Exact nonlinear plasma oscillations. *Phys. Rev.*, 108:546–550, 1957.
- [6] C. K. Birdsall and A. B. Langdon. *Plasma physics via computer simulation*. Institute of Physics Publishing, 1991.
- [7] J. Boris and D. Book. Solution of continuity equations by the method of flux-corrected transport. *J. Comp. Phys.*, 20:397–431, 1976.
- [8] C. Z. Cheng and G. Knorr. The integration of the Vlasov equation in configuration space. *Journal of Computational Physics*, 22(3):330–351, 1976.
- [9] Y. Cheng and I. M. Gamba. Numerical study of Vlasov-Poisson equations for infinite homogeneous stellar systems. *Comm. Nonlin. Sci. Num. Sim.*, 17, 2012.
- [10] Y. Cheng, I. M. Gamba, and J. Proft. Positivity-preserving discontinuous Galerkin schemes for linear Vlasov-Boltzmann transport equations. *Math. Comp.*, 2010. to appear.
- [11] B. Cockburn, S. Hou, and C.-W. Shu. The Runge-Kutta local projection discontinuous Galerkin finite element method for conservation laws IV: the multidimensional case. *Math. Comput.*, 54:545–581, 1990.
- [12] B. Cockburn, S. Y. Lin, and C.-W. Shu. TVB Runge-Kutta local projection discontinuous Galerkin finite element method for conservation laws III: one dimensional systems. *J. Comput. Phys.*, 84:90–113, 1989.
- [13] B. Cockburn and C.-W. Shu. TVB Runge-Kutta local projection discontinuous Galerkin finite element method for conservation laws II: general framework. *Math. Comput.*, 52:411–435, 1989.
- [14] B. Cockburn and C.-W. Shu. The Runge-Kutta local projection p1-discontinuous Galerkin finite element method for scalar conservation laws. *Math. Model. Num. Anal.*, 25:337–361, 1991.
- [15] B. Cockburn and C.-W. Shu. The Runge-Kutta discontinuous Galerkin method for conservation laws V: multidimensional systems. *J. Comput. Phys.*, 141:199–224, 1998.
- [16] L. Demeio and P. F. Zweifel. Numerical simulations of perturbed Vlasov equilibria. *Phys. Fluids B*, 2:1252–1254, 1990.
- [17] E. G. Evstatiev and B. A. Shadwick. *J. Comp. Phys.*, preprint 2012. to appear.
- [18] E. Fijalkow. A numerical solution to the Vlasov equation. *Comput. Phys. Comm.*, 116:319–328, 1999.

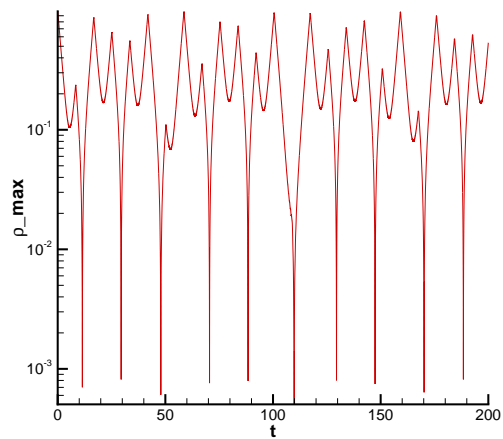
- [19] F. Filbet, E. Sonnendrücker, and P. Bertrand. Conservative numerical schemes for the Vlasov equation. *J. Comp. Phys.*, 172:166–187, 2001.
- [20] B. D. Fried and S. D. Conte. *The plasma dispersion function*. Academic Press, London, 1961.
- [21] R. T. Glassey. *The Cauchy problem in kinetic theory*. Society for Industrial and Applied Mathematics (SIAM), Philadelphia, PA, 1996.
- [22] R. E. Heath. Numerical analysis of the discontinuous Galerkin method applied to plasma physics. 2007. Ph. D. dissertation, the University of Texas at Austin.
- [23] R. E. Heath, I. M. Gamba, P. J. Morrison, and C. Michler. A discontinuous Galerkin method for the Vlasov-Poisson system. *J. Comp. Phys.*, 231:1140–1174, 2012.
- [24] R. W. Hockney and J. W. Eastwood. *Computer simulation using particles*. McGraw-Hill, New York, 1981.
- [25] T. W. Johnston, Y. Tyshetskiy, A. Ghizzo, and P. Bertrand. Persistent subplasma-frequency kinetic electrostatic electron nonlinear waves. *Phys. Plasmas*, 16:042105, 2009.
- [26] S. Jung, P. J. Morrison, and H. L. Swinney. On the statistical mechanics of two-dimensional turbulence. *J. Fluid Mech.*, 554:433–456, 2006.
- [27] A. J. Klimas. A method for overcoming the velocity space filamentation problem in collisionless plasma model solutions. *J. Comp. Phys.*, 68:202–226, 1987.
- [28] A. J. Klimas and W. M. Farrell. A splitting algorithm for Vlasov simulation with filamentation filtration. *J. Comp. Phys.*, 110:150–163, 1994.
- [29] R. H. Kraichnan and D. Montgomery. Two-dimensional turbulence. *Rep. Prog. Phys.*, 43:548–618, 1980.
- [30] M. D. Kruskal and C. Oberman. On the stability of plasma in static equilibrium. *Phys. Fluids*, 1:275–280, 1958.
- [31] T. D. Lee. On some statistical properties of hydrodynamical and magneto-hydrodynamical fields. *Q. Appl. Math.*, 10:69–74, 1952.
- [32] P. Lesaint and P.-A. Raviart. On a finite element method for solving the neutron transport equation. In *Mathematical aspects of finite elements in partial differential equations (Proc. Sympos., Math. Res. Center, Univ. Wisconsin, Madison, Wis., 1974)*, pages 89–123. Math. Res. Center, Univ. of Wisconsin-Madison, Academic Press, New York, 1974.
- [33] S. Montgomery, J. A. Cobble, J. C. Fernandez, R. J. Focia, R. P. Johnson, N. Renard-LeGalloudec, H. A. Rose, and D. A. Russell. Recent Trident single hot spot experiments: Evidence for kinetic effects, and observation of Langmuir decay instability cascade. *Phys. Plasmas*, 9:2311–2320, 2002.

- [34] P. J. Morrison. Hamiltonian description of the ideal fluid. *Rev. Mod. Phys.*, 70:467–521, 1998.
- [35] P. J. Morrison. Hamiltonian description of Vlasov dynamics: action-angle variables for the continuous spectrum. *Transport Theory and Statistical Physics*, 29:397–414, 2000.
- [36] P. J. Morrison and D. Pfirsch. Free Energy Expressions for Vlasov-Maxwell Equilibria. *Phys. Rev.*, 40A:3898–3910, 1989.
- [37] P. J. Morrison and D. Pfirsch. The free energy of Maxwell-Vlasov equilibria. *Phys. Fluids*, 2B:1105–1113, 1990.
- [38] P. J. Morrison and D. Pfirsch. Dielectric energy versus plasma energy, and Hamiltonian action-angle variables for the Vlasov equation. *Phys. Fluids*, 4B:3038–3057, 1992.
- [39] J. Moser. Periodic orbits near an equilibrium and a theorem by Alan Weinstein. *Comm. Pure App. Math.*, 29:727–747, 1976.
- [40] F. T. M. Nieuwstadt and J. A. Steketee. *Selected papers of J. M. Burgers*. Kluwer Academic Publishers, Dordrecht, 1995.
- [41] J.-M. Qiu and C.-W. Shu. Positivity preserving semi-Lagrangian discontinuous Galerkin formulation: theoretical analysis and application to the Vlasov-Poisson system. 2011. submitted to J. Comp. Phys.
- [42] W. Reed and T. Hill. Triangular mesh methods for the neutron transport equation. Technical report, Los Alamos National Laboratory, Los Alamos, NM, 1973.
- [43] J. Rossmanith and D. Seal. A positivity-preserving high-order semi-Lagrangian discontinuous Galerkin scheme for the Vlasov-Poisson equations. 2011. submitted to J. Comp. Phys.
- [44] C.-W. Shu and S. Osher. Efficient implementation of essentially non-oscillatory shock-capturing schemes. *J. Comput. Phys.*, 77:439–471, 1988.
- [45] E. Sonnendrücker, J. Roche, P. Bertrand, and A. Ghizzo. The semi-Lagrangian method for the numerical resolution of the Vlasov equation. *J. Comp. Phys.*, 149(2):201–220, 1999.
- [46] F. Valentini, T. M. O’Neil, and D. H. E. Dubin. Excitation of nonlinear electron acoustic waves. *Phys. Plasmas*, 13:052303, 2006.
- [47] F. Valentini, D. Perrone, F. Califano, F. Pegoraro, P. Veltri, P. J. Morrison, and T. M. O’Neil. Undamped electrostatic plasma waves. *Phys. Plasmas*, 19:092103, 2012.
- [48] Y. Xing, X. Zhang, and C.-W. Shu. Positivity preserving high order well balanced discontinuous Galerkin methods for the shallow water equations. *Advances in Water Resources*, 33:1476–1493, 2010.

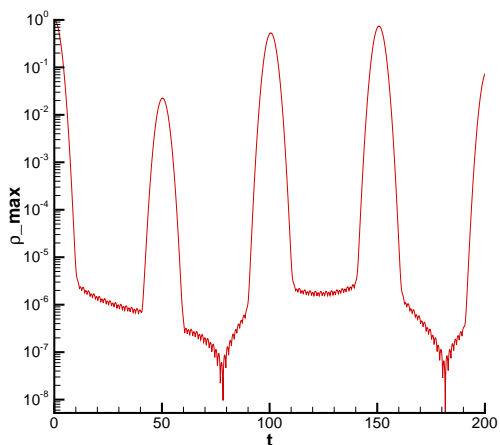
- [49] S. Zaki, L. Gardner, and T. Boyd. A finite element code for the simulation of one-dimensional Vlasov plasmas. i. theory. *J. Comp. Phys.*, 79:184–199, 1988.
- [50] S. Zaki, L. Gardner, and T. Boyd. A finite element code for the simulation of one-dimensional Vlasov plasmas. ii. applications. *J. Comp. Phys.*, 79:200–208, 1988.
- [51] M. Zhang and C.-W. Shu. An analysis of and a comparison between the discontinuous Galerkin and the spectral finite volume methods. *Computers and Fluids*, 34:581–592, 2005.
- [52] X. Zhang and C.-W. Shu. On maximum-principle-satisfying high order schemes for scalar conservation laws. *J. Comput. Phys.*, 229:3091–3120, 2010.
- [53] X. Zhang and C.-W. Shu. On positivity preserving high order discontinuous Galerkin schemes for compressible Euler equations on rectangular meshes. *J. Comput. Phys.*, 229:8918–8934, 2010.
- [54] X. Zhang and C.-W. Shu. Maximum-principle-satisfying and positivity-preserving high order schemes for conservation laws: Survey and new developments. *Proceedings of the Royal Society A*, 2011. to appear.
- [55] X. Zhang and C.-W. Shu. Positivity-preserving high order discontinuous Galerkin schemes for compressible Euler equations with source terms. *J. Comput. Phys.*, 230:1238–1248, 2011.
- [56] X. Zhang, Y. Xia, and C.-W. Shu. Maximum-principle-satisfying and positivity-preserving high order discontinuous Galerkin schemes for conservation laws on triangular meshes. *J. Sci. Comp.* to appear.
- [57] X. Zhong and C.-W. Shu. Numerical resolution of discontinuous galerkin methods for time dependent wave equations. 200:2814–2827, 2011.
- [58] T. Zhou, Y. Guo, and C.-W. Shu. Numerical study on Landau damping. *Physica D: Nonlinear Phenomena*, 157(4):322–333, 2001.



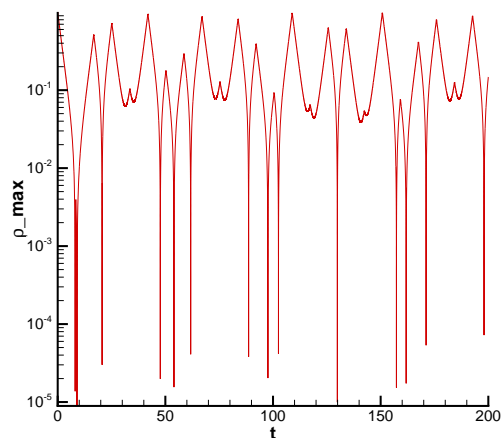
(a) Maxwellian, \mathbb{Q}^1



(b) Lorentzian, \mathbb{Q}^1

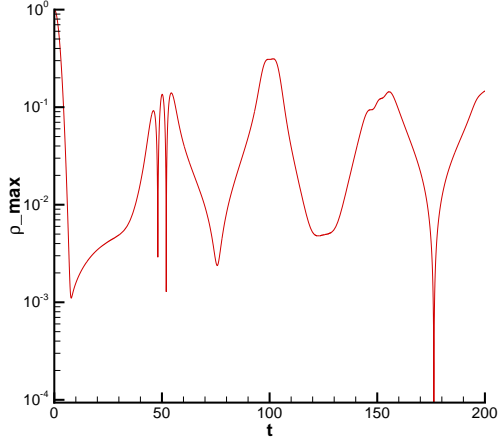


(c) Maxwellian, \mathbb{Q}^2

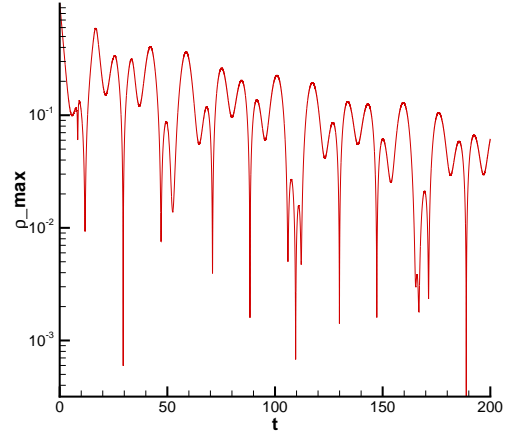


(d) Lorentzian, \mathbb{Q}^2

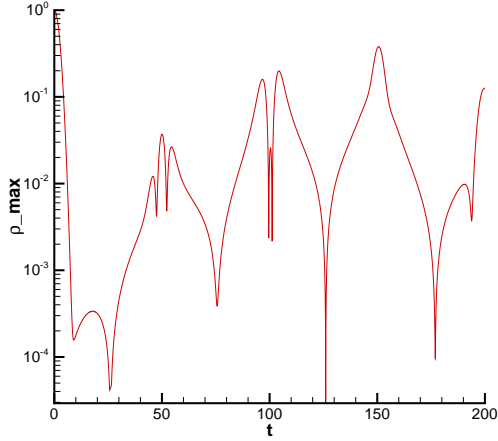
Figure 2: Computations of the advection equation for the polynomial spaces \mathbb{Q}^1 and \mathbb{Q}^2 showing local maxima of the density ρ_{max} as a function of time. The mesh is 40×40 with $\Delta x = \pi/10$. For the Maxwellian equilibrium $\Delta v = 1/4$, while for the Lorentzian equilibrium $\Delta v = 3/2$.



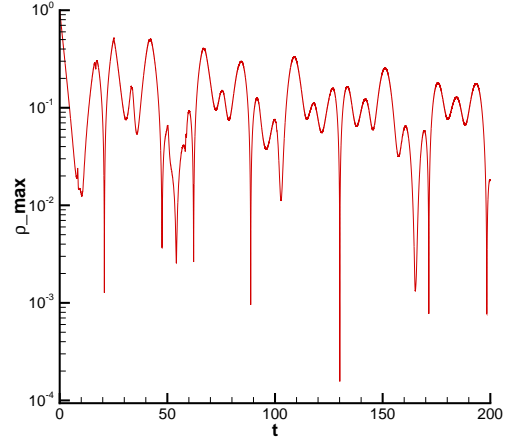
(a) Maxwellian, \mathbb{P}^1



(b) Lorentzian, \mathbb{P}^1



(c) Maxwellian, \mathbb{P}^2



(d) Lorentzian, \mathbb{P}^2

Figure 3: Computations of the advection equation for the polynomial spaces \mathbb{P}^1 and \mathbb{P}^2 showing local maxima of the density ρ_{max} as a function of time. The mesh is 40×40 with $\Delta x = \pi/10$. For the Maxwellian equilibrium $\Delta v = 1/4$, while for the Lorentzian equilibrium $\Delta v = 3/2$.

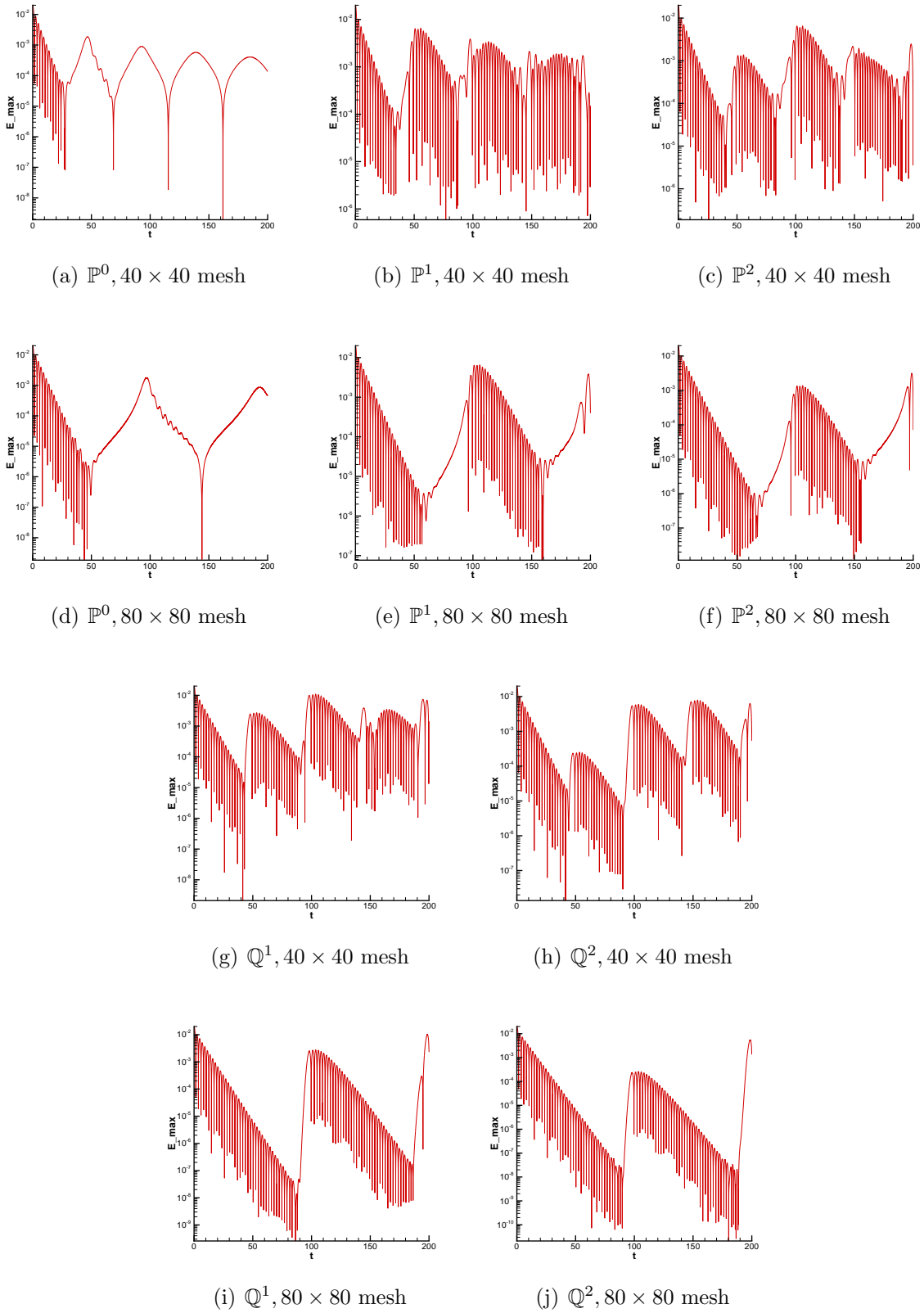


Figure 4: Depiction of linear Landau damping showing recurrence in the maxima of the electric field, E_{max} , as a function of time for various polynomial spaces.

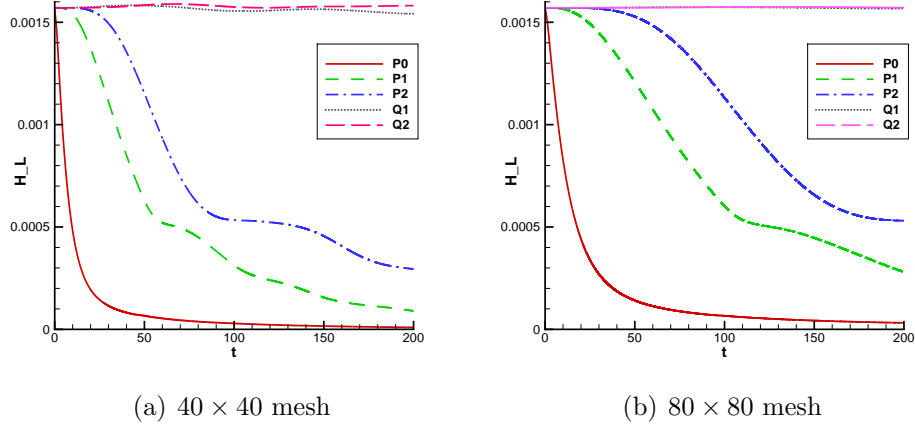


Figure 5: Evolution of the linear energy H_L of (16) as a function of time, while the Vlasov system undergoes linear Landau damping. Various polynomial spaces and mesh sizes were used, as indicated.

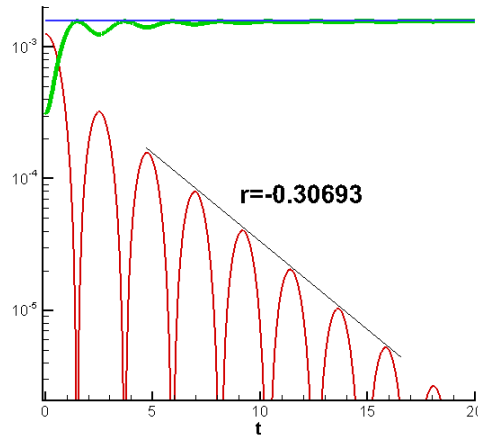


Figure 6: Evolution of the electrostatic energy (red), linear energy (blue) and the first term in the linear energy (green) as a function of time, while the Vlasov system undergoes linear Landau damping. Here Q^2 was used with a 80×80 mesh.

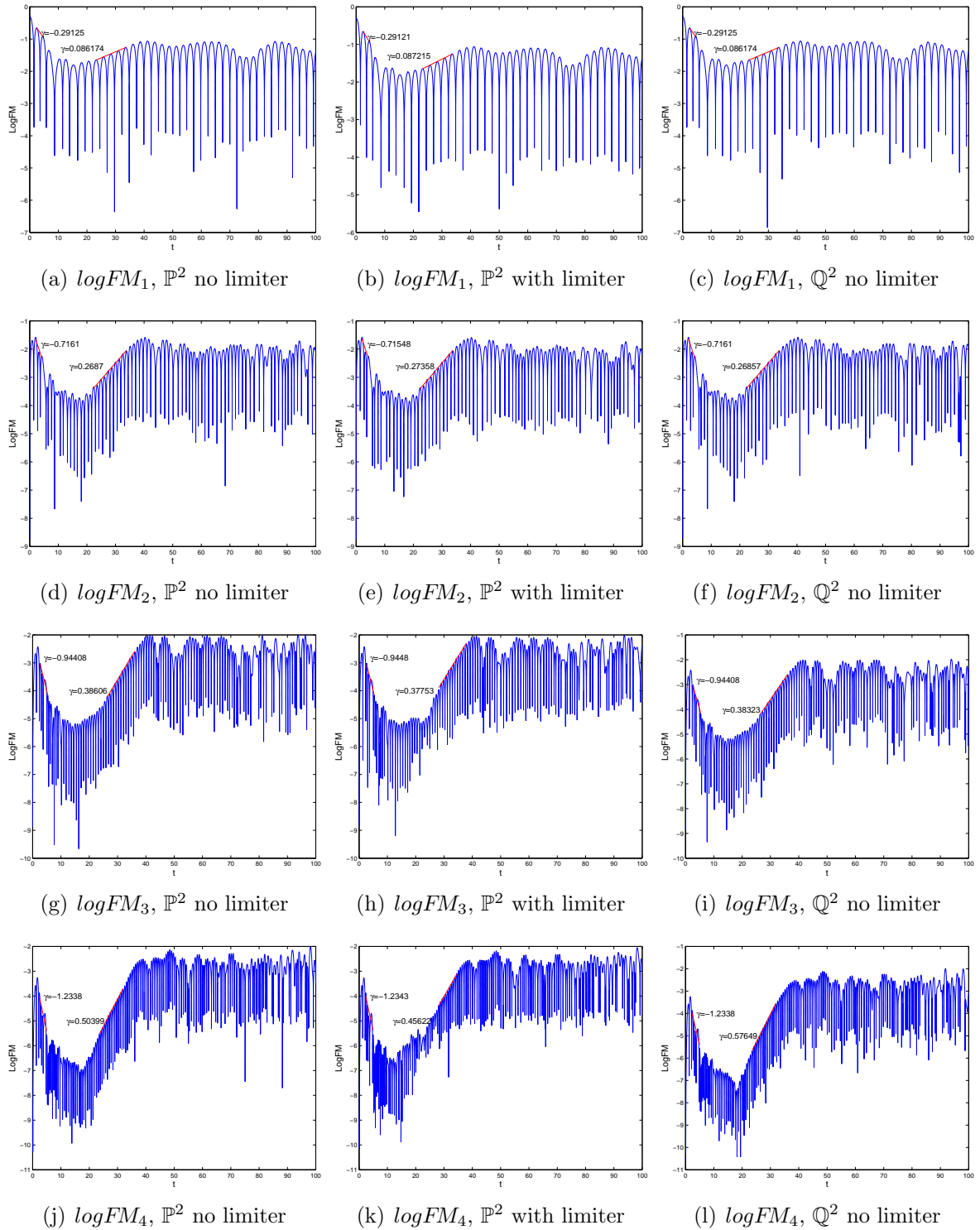
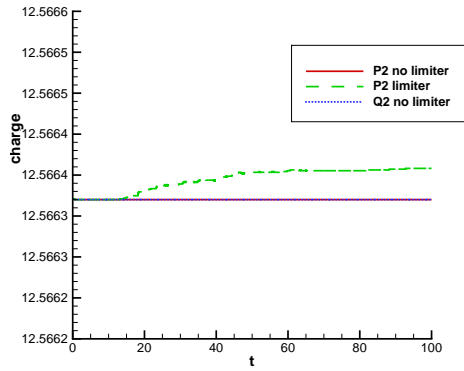
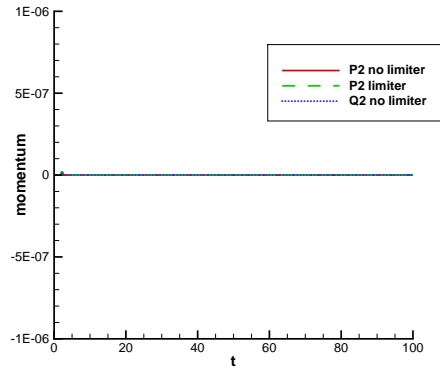


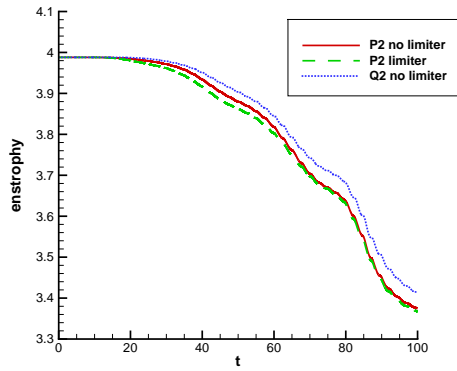
Figure 7: Evolution of the first four Log Fourier mode as a function of time for nonlinear Landau damping. Various values of the numerical damping/growth rate are marked on the graphs. Here the \mathbb{P}^2 space with the positivity-preserving limiter was used on a 100×200 mesh. The predicted recurrence time T_R for $\log FM_1$ is 209.44, for $\log FM_2$ is 104.72, for $\log FM_3$ is 69.81, and for $\log FM_4$ is 52.36.



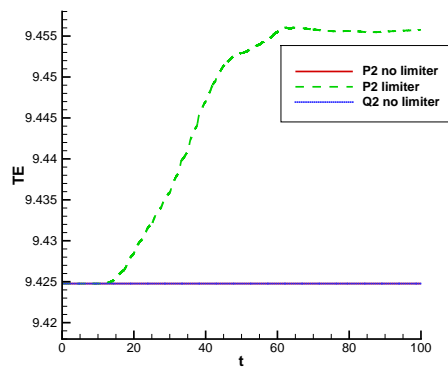
(a) charge



(b) momentum

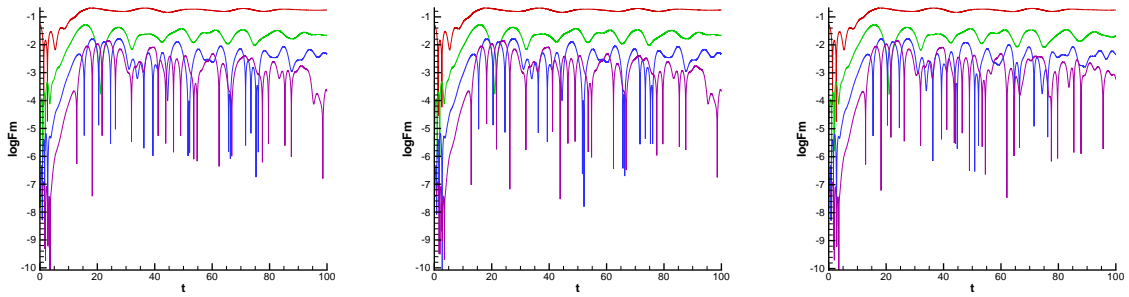


(c) enstrophy

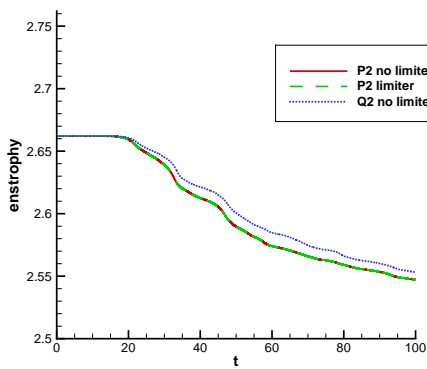


(d) total energy

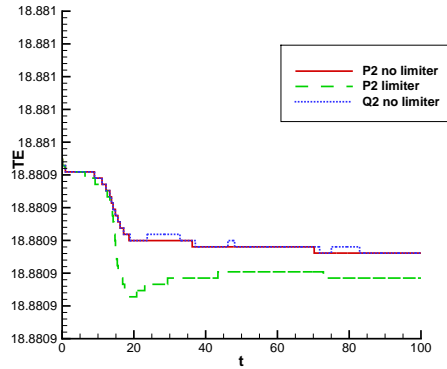
Figure 8: Evolution of conserved quantities as a function of time during the course of nonlinear Landau damping for various computational methods. A mesh of 100×200 was used.



(a) $\log FM_{1,2,3,4}, \mathbb{P}^2$ no limiter (b) $\log FM_{1,2,3,4}, \mathbb{P}^2$ with limiter (c) $\log FM_{1,2,3,4}, \mathbb{Q}^2$ no limiter



(d) enstrophy



(e) total energy

Figure 9: Depiction of the first four Log Fourier modes during the nonlinear evolution of the two-stream instability. Also depicted is the evolution of energy and enstrophy as a function of time for various methods.

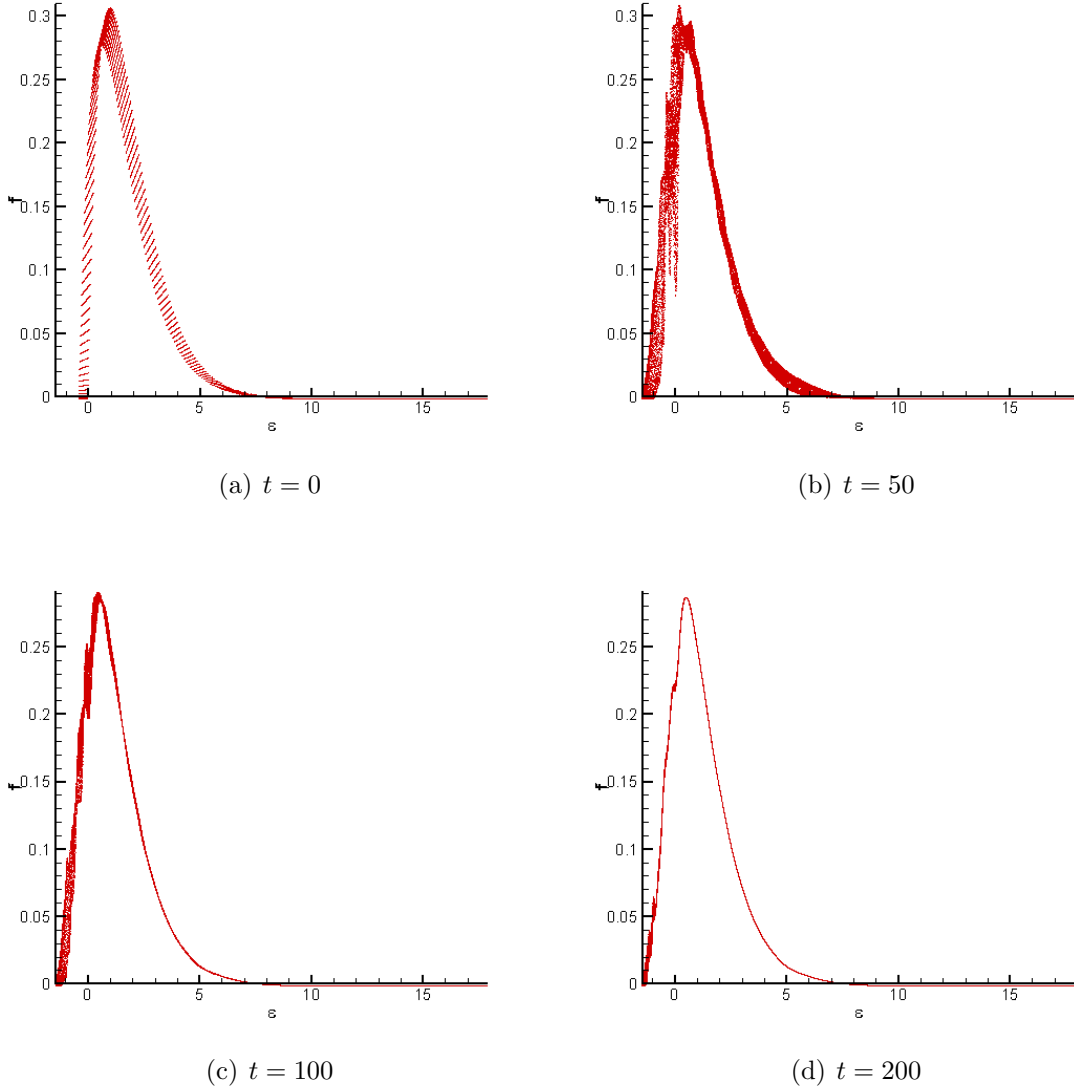


Figure 10: Plots of the distribution $f(x, v, t)$ versus $\epsilon = \frac{v^2}{2} - \Phi(x, t)$ for the two-stream instability at the times t indicated, showing saturation to a BGK state. Here the \mathbb{P}^2 space with the positivity-preserving limiter was used on a 100×200 mesh.

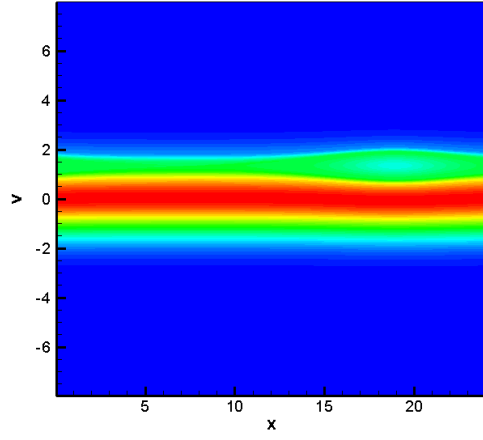


Figure 11: Phase space contour at $T = 1000$ for with DA initial condition with drive A_d^J . The plot suggests saturation to a moving BGK-like state. Here the \mathbb{Q}^1 element was used on a 200×400 mesh.

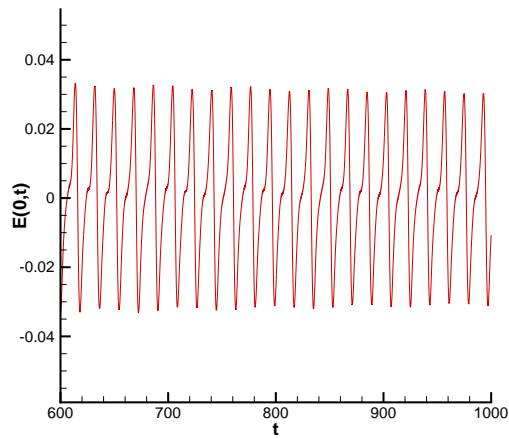


Figure 12: The electric field $E(0,t)$ at the center of the spacial domain at late times for the drive A_d^J . The periodicity matches the propagation of the BGK-like state through the domain. Here the \mathbb{Q}^1 element was used on a 200×400 mesh.

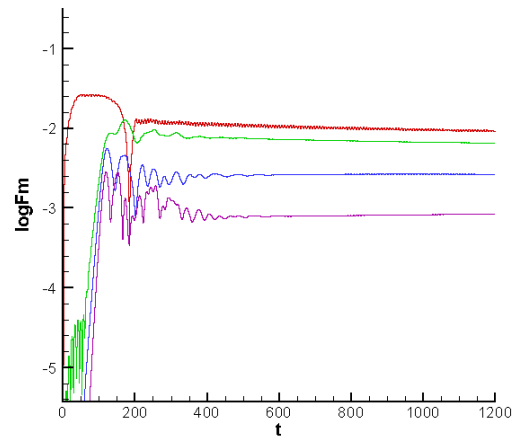


Figure 13: The first four Log Fourier Modes for the drive A_d^J , indicating saturation. Here the Q^1 element was used on a 200×400 mesh.

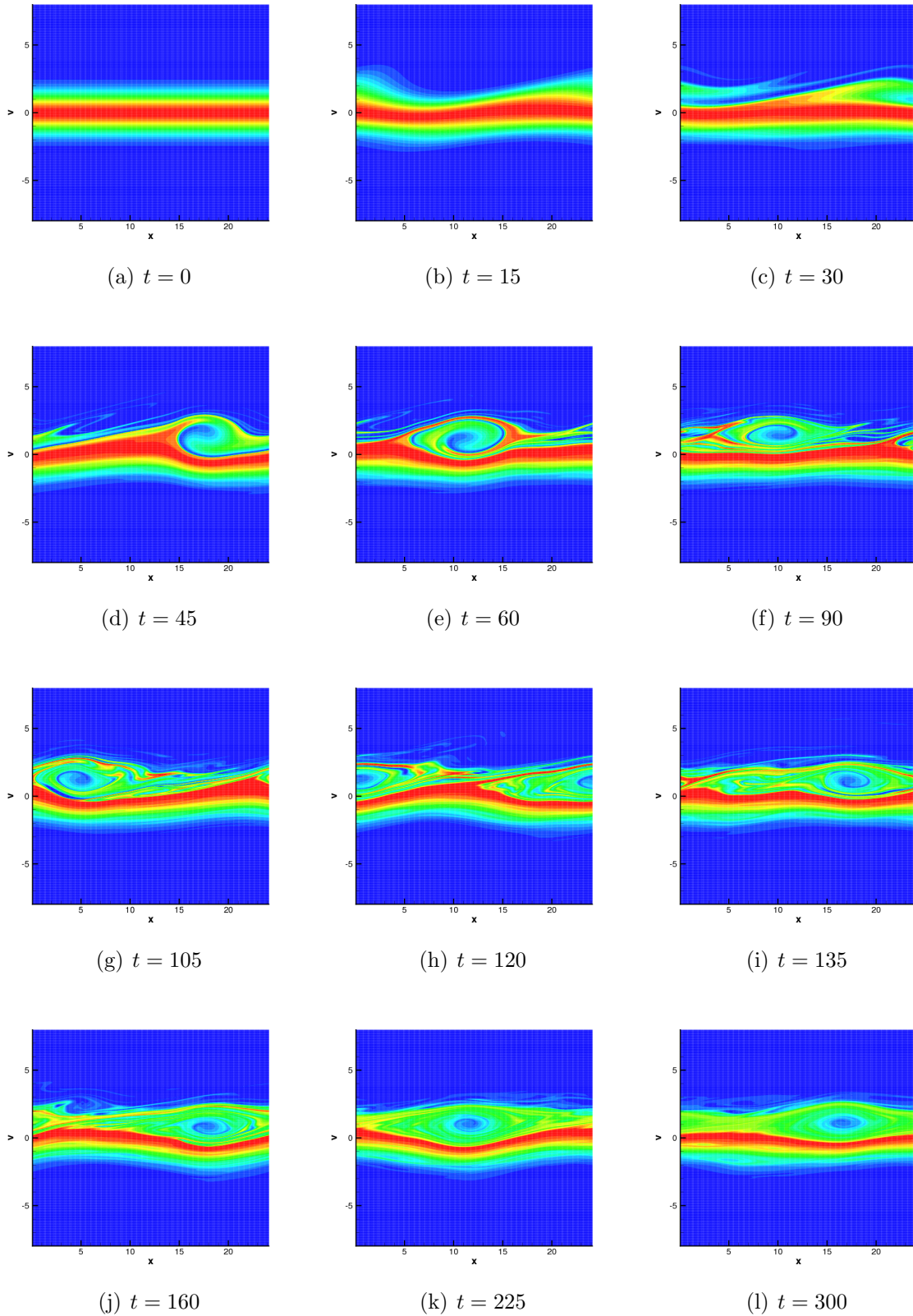


Figure 14: Phase space contour plots for the KEEN wave at the times indicated. A large amplitude drive of $A_m = 0.4$ was used, along with the \mathbb{P}^2 basis and a positivity-preserving limiter on a 200×400 mesh.

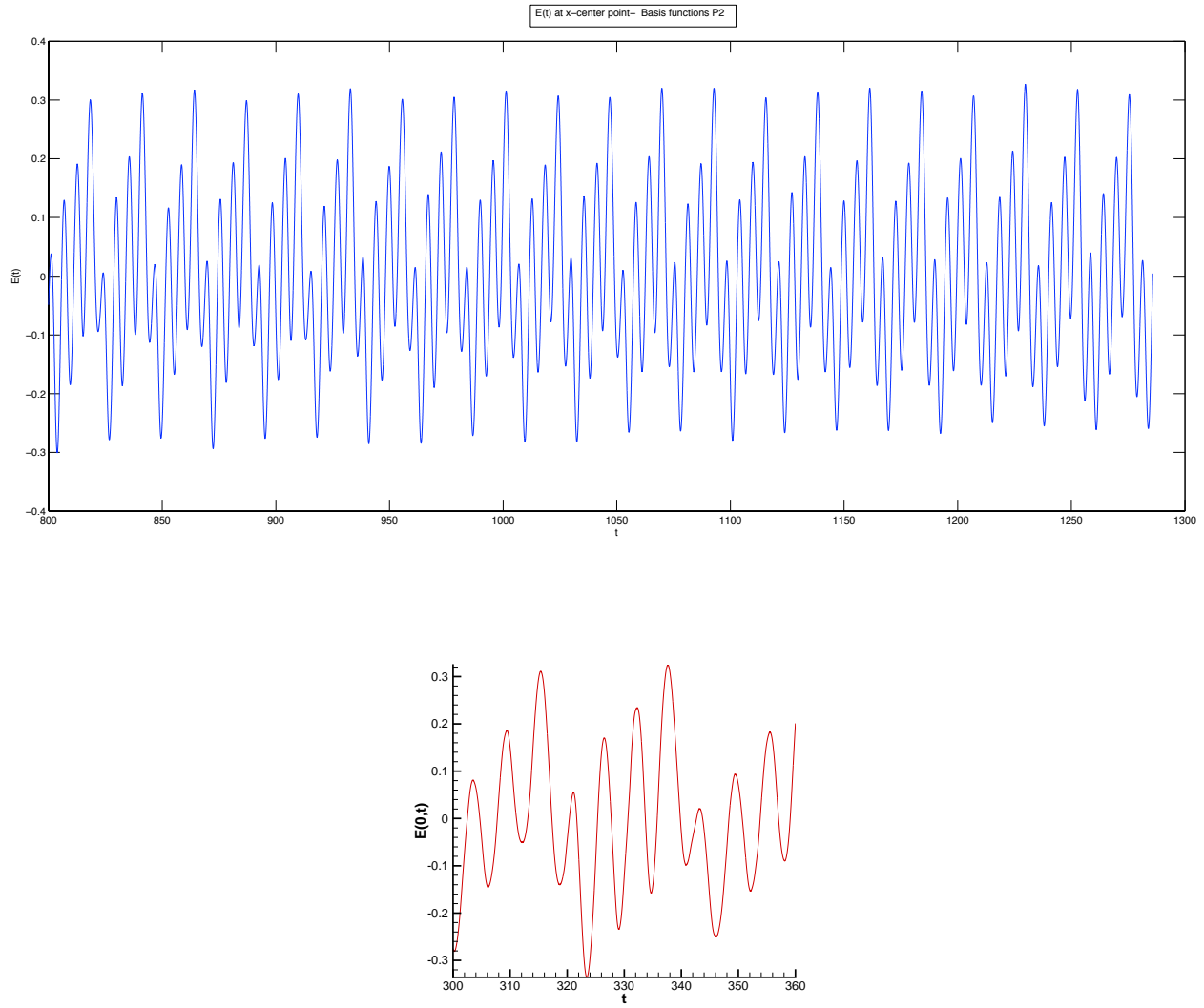


Figure 15: (*top*) The electric field $E(0,t)$ at the center of the spacial domain at later times for the drive A_d^A . The periodic structure is due to multiple interacting BGK-like states. (*bottom*) Blow up indicating a period-4 modulation of a central hole such as that of Fig. 12). The simulation was done with \mathbb{P}^2 elements with a limiter on a 200×400 mesh.

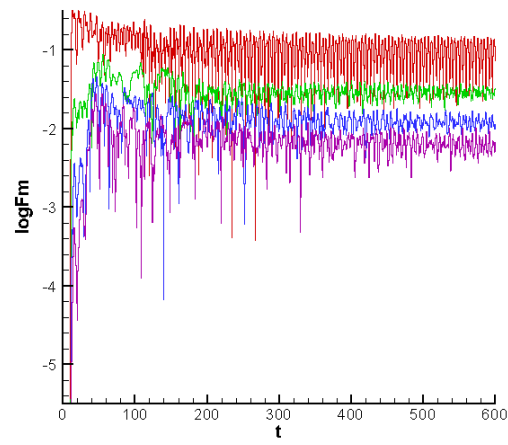


Figure 16: Evolution of the first four Log Fourier modes as a function of time for the drive of Eq. (18). The simulation used \mathbb{P}^2 elements with a limiter on a 200×400 mesh.